J. Fluid Mech. (2018), *vol.* 847, *pp.* 28–70.
doi:10.1017/jfm.2018.257

Numerical study of turbulent separation bubbles with varying pressure gradient and Reynolds number

G. N. Coleman[1,†], C. L. Rumsey[1] and P. R. Spalart[2]

[1]Computational AeroSciences, NASA Langley Research Center, Hampton, VA 23681, USA

[2]Boeing Commercial Airplanes, Seattle, WA 98124, USA

(Received 26 October 2017; revised 16 February 2018; accepted 17 March 2018; first published online 17 May 2018)

A family of cases each containing a small separation bubble is treated by direct numerical simulation (DNS), varying two parameters: the severity of the pressure gradients, generated by suction and blowing across the opposite boundary, and the Reynolds number. Each flow contains a well-developed entry region with essentially zero pressure gradient, and all are adjusted to have the same value for the momentum thickness, extrapolated from the entry region to the centre of the separation bubble. Combined with fully defined boundary conditions this will make comparisons with other simulations and turbulence models rigorous; we present results for a set of eight Reynolds-averaged Navier–Stokes turbulence models. Even though the largest Reynolds number is approximately 5.5 times higher than in a similar DNS study we presented in 1997, the models have difficulties matching the DNS skin friction very closely even in the zero pressure gradient, which complicates their assessment. In the rest of the domain, the separation location *per se* is not particularly difficult to predict, and the most definite disagreement between DNS and models is near reattachment. Curiously, the better models tend to cluster together in their predictions of pressure and skin friction even when they deviate from the DNS, although their eddy-viscosity levels are widely different in the outer region near the bubble (or they do not rely on an eddy viscosity). Stratford's square-root law is satisfied by the velocity profiles, both at separation and reattachment. The Reynolds-number range covers a factor of two, with the Reynolds number based on the extrapolated momentum thickness equal to approximately 1500 and 3000. This allows tentative estimates of the improvements that even higher values will bring to the model comparisons. The solutions are used to assess models through pressure, skin friction and other measures; the flow fields are also used to produce effective eddy-viscosity targets for the models, thus guiding turbulence-modelling work in each region of the flow.

Key words: boundary layer separation, turbulence modelling, turbulence simulation

1. Introduction: background and objectives

This study considers the pressure-gradient-induced separation and reattachment of flat-plate turbulent boundary layers. It is a continuation, both in terms of its topic and

† Email address for correspondence: g.n.coleman@nasa.gov

approach, of our earlier work (Spalart & Coleman 1997; henceforth denoted SC97), which used direct numerical simulation (DNS) of a single configuration at, arguably, a marginal Reynolds number although the flow was definitely turbulent. Computational resources now allow DNS of multiple separation bubbles, created by sudden and more gradual pressure gradients, at Reynolds numbers much higher, and in domains much larger, than reachable to SC97. Other simulations of the separation-bubble configuration include Na & Moin's (1998) DNS from the same era (see also Skote & Henningson 2002) and Abe's (2017) DNS, as well as Raiesi, Piomelli & Pollard's (2011) and Cheng, Pullin & Samtaney's (2015) large-eddy simulations (LES). Abe's flow fields (and approach) are very similar to ours, but unfortunately at somewhat different conditions. Primarily addressing the behaviour of wall-pressure fluctuations, Abe did vary the pressure-gradient strength to some extent, and covered a factor of three in Reynolds number (up to 900, based on upstream/inflow momentum thickness), observing the strongest *Re* effects near reattachment. The flow with laminar separation and turbulent reattachment has been addressed by Alam & Sandham (2000) and Spalart & Strelets (2000), and is quite different.

In engineering applications relevant to the air, sea or ground, the critical role played by turbulent-boundary-layer separation – via its power to set optimal design conditions, to make distant regions of the flow sensitive to each other and thereby to severely challenge turbulence models by taking them far away from their training grounds – is well established (Slotnick *et al.* 2014). The present focus is upon the small separation bubble that results from subjecting a well-defined zero-pressure-gradient (ZPG) turbulent layer to a prolonged adverse pressure gradient (APG), followed shortly after the mean-flow reversal, by a favourable gradient (FPG) and another ZPG, of long enough duration to allow the boundary layer to recover toward the canonical ZPG state. The APG region will display departures from the log law, which will be either general or progressive (Galbraith, Sjolander & Head 1977). This admittedly constrained configuration is motivated by the perennial limitations on the volume of turbulence capturable by DNS. For instance, DNS of a circular-cylinder flow is possible, without precipitating reattachment, but typically at Reynolds numbers of a few thousand based on diameter; here the Reynolds number is of a few thousand based on boundary-layer thickness, so that we are emulating the boundary layer in a flow that could have a longitudinal Reynolds number in the million range. We do note the impressive cylinder and sphere simulations of Rodriguez *et al.* (2014), which approach the million mark based on diameter and reproduce the 'rich kaleidoscope of fluid-mechanic phenomena' Mark Morkovin described so eloquently. These simulations are labelled as LES, but we speculate that the key region, which mingles separation and transition, comes close to DNS.

The present flow is devoid of any features of compressibility (in contrast with the Bachalo–Johnson (1986) transonic shock-induced separation) or surface variation, either gradual (as in the NASA wall-mounted hump experiment; Naughton, Viken & Greenblatt 2006; Uzun & Malik 2017) or sudden (as in the backward-facing-step or surface-mounted-cube flows; e.g. Castro & Robins 1977; Driver & Seegmiller 1985; Le, Moin & Kim 1997; Yakhot *et al.* 2006). On the other hand, in a continuation paper we will present results with sweep, motivated by the definite three-dimensionality of many key boundary layers, on aircraft, on vehicles, on wind turbines and so on. In fact we speculate that three-dimensional separation could be less difficult to predict, the near-wall turbulence still being driven by a non-zero skin-friction vector.

An essential requirement of this study is to provide precise boundary conditions, and also a precise characterisation of the ZPG entry region as a fully developed

turbulent layer with essentially no memory of how the turbulence was generated, so that specifying the boundary-layer thickness is sufficient information for any comparison, be it with another DNS, LES, Reynolds-averaged Navier–Stokes (RANS) solutions or even an experiment. (This strategy was pioneered, in an experimental context, by Driver & Johnston (1990) and Driver (1991), in their studies of separation in axisymmetric boundary-layer flow over longitudinal cylinders.)

An auxiliary interest is in the square-root velocity profile proposed by Stratford (1959) at separation, which in other work we have found to be quite successful (Coleman *et al.* 2017). A key consideration is that our other study was of a Couette–Poiseuille flow, independent of streamwise direction x in the mean, with sustained zero skin friction; compare this with Stratford's original flow, with sustained zero skin friction but a rapidly thickening boundary layer, and the present situation in which the skin friction merely crosses zero in one direction and then the other. The resilience, if any, of the square-root law and its constants to these rather significant differences is of deep theoretical interest.

The primary measures of this family of flows are the usual wall pressure and skin-friction distributions, followed by velocity and Reynolds-stress profiles. These result from the behaviour of the turbulence in the entire domain surrounding the bubble, so that specific deviations of a model are difficult to identify. Another direction of effort is attempts to assess the behaviour of RANS models locally. Such guidance could potentially inspire substantial improvements, even if it is used 'manually', as opposed to by machine learning. As in Raiesi *et al.* (2011) (see also Abe *et al.* 2012), a primary element of this style of work is the definition of an effective eddy viscosity, giving a single target for models at each point, rather than inspecting all six Reynolds stresses and trying to identify the pivotal one. (For instance, in unidirectional flows with e.g. U solely as a function of y, the shear stress $-\overline{u'v'}$ is the only one to have any effect, but this is not true in a fully two-dimensional flow.) We demonstrate below that this scalar eddy viscosity does not return the exact DNS flow field when introduced into the momentum equation, presumably because the linear Boussinesq, or even the nonlinear, constitutive relations have their own errors, but it is a sound first step. Even though this quantity is local, history effects and the interplay between the relatively numerous terms in the models make it far from trivial to decide which term to alter, and RANS modelling still demands a lot of judgment. Naturally, a central difficulty resides in improving the accuracy in the present flow or flow family, while satisfying the fundamental invariance requirements and without damaging the accuracy in the key past calibration cases. Another exercise, also aimed at bringing out local failures of the models, consists of solving the transport and constitutive equations of the models by using the mean velocity field from the DNS wherever it appears in the closure, without applying the momentum equation. This makes the comparison with the DNS effective eddy viscosity even more direct; it is employed below, and the results are contrasted with the eddy-viscosity field diagnosed from the DNS.

The numerical approach and parameters used for the DNS are described in § 2 (with specialist details given in appendices A and B) – relating how the simulations were done, how confidence in their accuracy was established and how the data can be accessed. The DNS results are presented in § 3 (and appendix C) – addressing fundamental questions and turbulence theory. Section 4 contains a RANS-model study – examining the ability of a range of commonly used computational fluid dynamics (CFD) models to reproduce the DNS data. The summary and closing remarks offered in § 5 recap the major findings and practical implications of this study, and state our future plans.

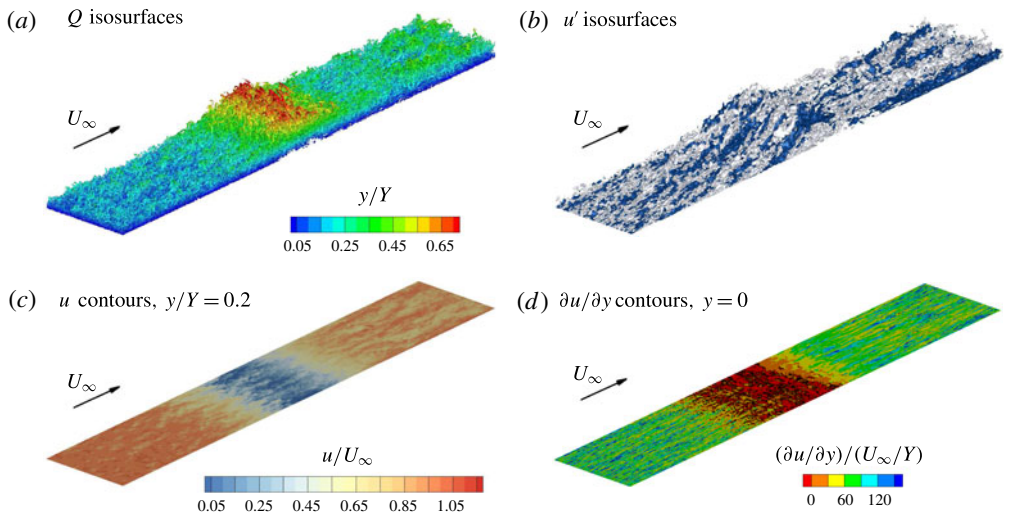

FIGURE 1. Subdomain Case A visualisations of (*a*) $Q \equiv -(1/2)(\partial u_i/\partial x_j)(\partial u_j/\partial x_i) = 5U_\infty^2/Y^2$ isocontours, coloured by wall-normal coordinate y, (*b*) isocontours of streamwise velocity perturbation u', relative to local spanwise averaged velocity (dark, $u' = -0.1U_\infty$; light, $u' = +0.1U_\infty$), (*c*) streamwise velocity at $y/Y = 0.2$ (i.e. 20 % of the distance between the no-slip surface and height at which transpiration boundary condition is applied) and (*d*) wall-normal gradient of streamwise velocity $\partial u/\partial y$ at $y = 0$ (black lines, $\partial u/\partial y = 0$; red contours, $\partial u/\partial y < 0$). Subdomain shown is from $x/Y = -5.5$ to 5.5 and $z/Y = 0$ to 2 (i.e. 42 % and 50 % respectively of the full $-11.5 \leqslant x/Y \leqslant 14.5$ and $0 \leqslant z/Y \leqslant 4$ domain). Visualisation of detail may require expansion of online version of figure.

2. Approach

2.1. *Problem formulation and numerical strategy*

As in SC97, the flow in question is a fully turbulent incompressible ZPG boundary layer over a flat no-slip surface, subjected to first adverse then favourable mean streamwise pressure gradients. The pressure gradients are induced by a transpiration profile $V_{top}(x)$ through a virtual parallel plane offset a fixed distance Y from the no-slip surface. Instantaneous realisations of off-the-wall and near-wall turbulence structures for one of the cases are illustrated in figure 1. Corresponding mean-flow contours and streamlines are shown in figure 2.

The strength and duration of the pressure gradients are controlled via the maximum velocity V_{max} and length scale σ of the transpiration profile, where

$$V_{top}(x) = -\sqrt{2}V_{max}\left[\frac{x}{\sigma}\right]\exp\left(\frac{1}{2} - \left[\frac{x}{\sigma}\right]^2\right) + \varphi_{top}, \tag{2.1}$$

with $x = 0$ defined as the location at which V_{top} changes from suction to blowing (see figure 3*a*). This profile (the derivative of a Gaussian) is associated with a bell-shaped streamwise variation of static pressure (see figure 3*b* and below). The last term in (2.1), φ_{top}, is a (small) constant 'bleed' velocity, adjusted to offset the blockage in the (nominally) ZPG regions, and thereby produce $\mathrm{d}P/\mathrm{d}x \approx 0$ along the wall there.

The procedure used to impose the transpiration profile at $y = Y$ in a periodic/semi-infinite spectral algorithm will be described below. An equivalent alternative to what

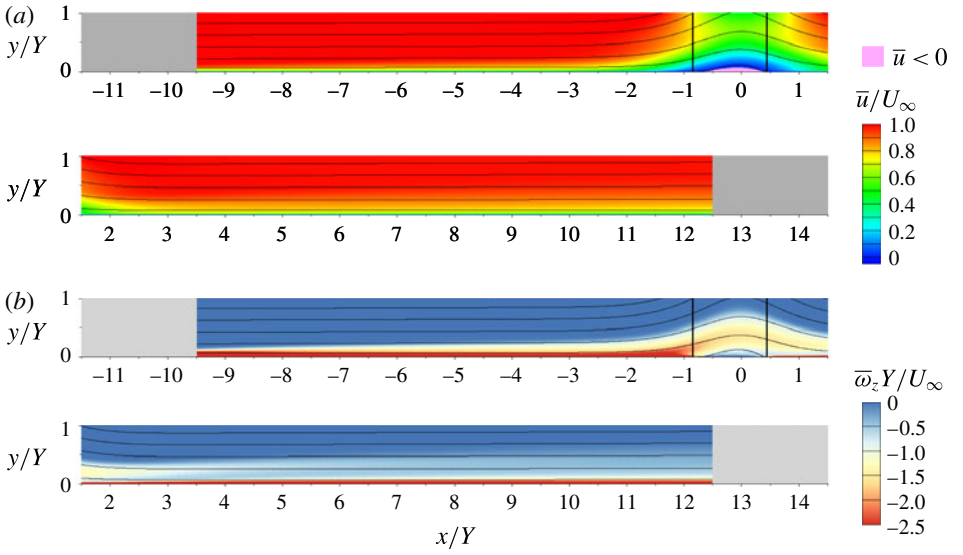

FIGURE 2. Contours of mean streamlines and (*a*) streamwise velocity $\overline{u}$ and (*b*) spanwise vorticity $\overline{\omega}_z$ for Case A. Shaded/grey regions at in/outflow of domain are fringe zones. Solid vertical lines indicate mean separation and reattachment locations. Subdomain below $y = Y$ shown.

follows is to specify the irrotational transpiration boundary conditions at $y = Y$ as

$$v = V_{top}(x), \quad \frac{\partial u}{\partial y} = \frac{\mathrm{d}V_{top}}{\mathrm{d}x}, \quad \frac{\partial w}{\partial y} = 0. \tag{2.2a–c}$$

These conditions could be applied in DNS, LES or RANS calculations that use a finite domain in the wall-normal direction; for a RANS calculation, they correspond to, for example, $\overline{v'v'} = \partial\overline{u'u'}/\partial y = 0$. (Some RANS models may need additional conditions for their dependent variables, especially if they involve pressure.)

The present solutions are obtained using the fully spectral scheme of Spalart, Moser & Rogers (1991), with mean streamwise variations accommodated by the 'fringe method' introduced by Spalart & Watmuff (1993) (cf. shaded regions in figure 2); see appendix A. Note that the top of the computational domain is not at $y = Y$: the domain is semi-infinite in the wall-normal direction y (between a no-slip wall at $y = 0$ and $y \to \infty$), and periodic in the streamwise x and spanwise z directions. The wall-normal basis functions involve Jacobi polynomials in $\zeta \in [0, 1]$, mapped to the $y \in [0, \infty]$ domain via $\zeta = \exp(-y/y_0)$, where y_0 is the mapping length scale. Apart from the alterations to the fringe treatment described in appendix A, the implementation is equivalent to that described in SC97, to which the reader is referred for details. For present purposes, we note that the strategy (first applied to a non-separating turbulent APG boundary layer, by Spalart & Watmuff (1993), and later to a laminar separation/turbulent reattachment by Spalart & Strelets (2000)) involves decomposing the velocity field $\boldsymbol{U}$ into three components: the 'vortical' computational variable $\boldsymbol{U}_1$, the fringe term $\boldsymbol{U}_2$ (see appendix A) and the field $\boldsymbol{U}_3$ by which the upper-wall transpiration-profile boundary condition is imposed (appendix B). The manner in which the three fields interact, and the alterations they introduce to the Navier–Stokes equations solved by the DNS code, is explained in SC97.

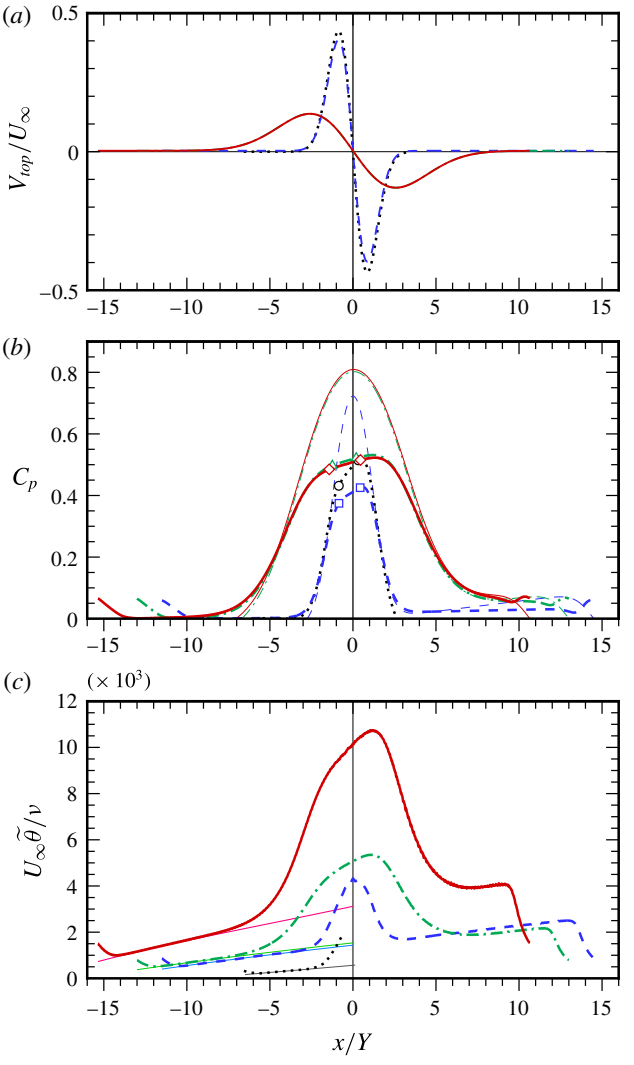

FIGURE 3. (Colour online) Streamwise variation of (*a*) transpiration profile along $y = Y$, (*b*) mean wall pressure and (*c*) momentum-thickness Reynolds number: ·····, SC97; - - - - (blue), Case A; — · — (green), Case B; —— (red), Case C. (Cases B and C results are identical in *a*.) Symbols in (*b*) correspond to mean separation and reattachment locations: ○, SC97; □ (blue), Case A; △ (green), Case B; ◇ (red), Case C. Thicker and thinner lines in (*b*) respectively indicate $(\overline{p}_{wall} - P_\infty)/(1/2)\rho U_\infty^2$ and the blockage-free wall-pressure variation $1-(U_{slip}/U_\infty)^2$, where U_{slip} is the irrotational slip velocity induced by V_{top} (see appendix B). Solid/thinner lines in (*c*) trace the virtual ZPG Reynolds-number variation, based on continuation of the ZPG region via either linear extrapolation (SC97) or, for Cases A–C, integration of a curve fit of the Coles (1962) ZPG boundary-layer data (see figure 5*b* and its legend). Results in (*c*) have been locally averaged in x.

2.2. *Cases and quality diagnostics*

The length Y and the free-stream value U_∞ of the ZPG boundary layer will be used to normalise most quantities. The principal non-dimensional parameters are summarised in table 1; the SC97 values are also included for reference. The transpiration

Case	$U_\infty Y/\nu$	$U_\infty\theta_0/\nu$	V_{max}/U_∞	σ/Y	φ_{top}/U_∞
SC97	22 000	565	0.4350	1.22	0
A	40 000	1437	0.4000	1.22	0.0034
B	40 000	1537	0.1333	3.66	0.0034
C	80 000	3121	0.1333	3.66	0.0034

TABLE 1. Case parameters.

parameters V_{max} and σ have been adjusted to produce a small separation bubble. For all three new cases, the transpiration strength $V_{max}\sigma$ is $0.49U_\infty Y$, which produces boundary layers whose thickness grows to be as much as 90 % of Y (figure 8*b*). For SC97, the $V_{max}\sigma$ product was slightly larger, $0.53U_\infty Y$, corresponding to a slightly deeper skin-friction reversal (figure 7). The momentum thickness θ_0 is a virtual quantity, namely the thickness extrapolated from the ZPG region to $x = 0$. For comparisons of cases at different Reynolds numbers and with different pressure gradients, all having different rates of growth for θ versus x, this appears to be a more relevant (albeit still somewhat arbitrary) measure than the thickness at a given distance upstream, say $x/Y = -5$. This illustrates the challenge of defining a true family of cases, particularly when attempting to isolate relatively subtle Reynolds-number effects, in contrast with simple channel studies for instance.

The suddenness of the separation-inducing APG is controlled by σ: Case A employs the same σ/Y as SC97, corresponding to a quite abrupt $\mathrm{d}P/\mathrm{d}x$, while for Cases B and C the pressure-gradient variation is more gradual, by way of a threefold increase in σ/Y relative to A and SC97 (compare figure 3*a*,*b*). Note that the current streamwise domain size is large enough to provide a significant ZPG/recovery region.

The $x = 0$ location of $V_{top}(x)$ (i.e. the streamwise station of the APG/FPG transition) varies from 44 to 59 % of Λ_x from the entrance to the (periodic) domain. This variation is a consequence of the strategy used to facilitate comparison of the new cases, which aimed to effect separation upon ZPG boundary layers with the same momentum thickness θ, extrapolated as explained above. The transpiration profile for each run was translated in x such that the virtual thickness of the ZPG layer (i.e. the thickness that would exist were the APG not applied) at $x = 0$, θ_0, is approximately the same for each case. The virtual momentum thickness is estimated by using the behaviour observed in the Coles (1962) experiments to extrapolate the streamwise variation of θ in the (pre-APG) ZPG region to the $x = 0$ location (see thin lines in figure 3*c*, which are based on the skin-friction versus momentum-thickness Reynolds number interpolant, $C_f = C_f(R_\theta)$, shown in figure 5*b*). The virtual R_θ at $x = 0$ is another defining characteristic of the DNS cases (see table 1). Values from 565 (SC97) to 3100 (C) are now available.

The numerical parameters are summarised in table 2. Based on the maximum skin friction τ_w over the 'useful region' (i.e. where the fringe terms are inactive; see figure 2), the spatial resolution for the three new cases is such that the maximum streamwise Δx and spanwise Δz spacings are respectively 13.5 and 6.2 wall units, while the tenth wall-normal collocation point y_{10} is at most $4.6\nu/u_\tau$ (the exponential-mapping length scale – see above – is $y_0 = 0.343Y$ for all cases, including the case presented in SC97). Given that $\Delta x^+ = \Delta u_\tau/\nu \approx 12\nu/u_\tau$ and $y_{10}^+ \approx 6$ are the threshold values for a fully spectral code, in terms of producing accurate first- and second-order statistics for wall-bounded turbulence (Spalart, Coleman & Johnstone

Case	Λ_x/Y	x_{in}/Y	x_{out}/Y	Λ_z/Y	N_x	Δx^+	N_y	y_{10}^+	N_z	Δz^+
SC97	10	−6.5	3.5	1.43	640	18.9	200	2.2	256	6.8
A	26	−11.5	14.5	4.0	3840	13.5	200	3.6	1280	6.2
B	26	−13.0	13.0	4.0	3840	13.4	200	3.6	1280	6.2
C	26	−15.35	10.65	4.0	7680	12.3	240	4.6	2560	6.0

TABLE 2. Numerical parameters. Origin of streamwise coordinate x, and thus locations of inflow x_{in} and outflow x_{out} stations, is defined by location of sign change of transpiration profile $V_{top}(x)$, with $x_{out} - x_{in} = \Lambda_x$, where Λ_x is the streamwise period of the domain (see figure 3*a* and main text); spanwise period is Λ_z. The reference velocity U_∞ and pressure P_∞ are defined at $(x, y) = (x_{in} + 2Y, 0.5Y)$. Dealiasing is enforced by defining the number of quadrature/collocation points, N_x, N_y and N_z, such that they are related to the number of streamwise, wall-normal and spanwise Galerkin spectral expansion coefficients, respectively, by $M_x = 2N_x/3$, $M_y = (2N_y - 9)/3$ and $M_z = 2N_z/3$. Spatial resolution is quantified in terms of the quadrature grid, such that $\Delta x = \Lambda_x/N_x$ and $\Delta z = \Lambda_z/N_z$; the distance y_{10} is that of the tenth wall-normal quadrature point from the bottom of the domain (with $y_1 = 0$). Wall units, e.g. $\Delta x^+ = \Delta x\, u_\tau/\nu$ and $y_{10}^+ = y_{10}\, u_\tau/\nu$, are based on maximum skin friction within the domain, downstream of the fringe zone, upstream of separation (figure 7*a*).

2009), the streamwise and especially wall-normal values for the near-wall regions of the new cases are adequate. On the other hand, the spanwise resolution is marginal in the ZPG region, since $\Delta z^+ \approx 4$ is required to ensure the near-wall structures are faithfully captured (cf. Spalart *et al.* 2009). However, for our present purposes this is not a serious problem: rerunning Case A with $N_z = 1920$, such that Δz^+ is reduced from 6.2 to 4.1, revealed at most a 2 % reduction in mean skin friction in the ZPG regions, and no discernible changes to the separation and reattachment locations, relative to the $\Delta z^+ \approx 6$ results presented below.

The other critical issue regarding spatial resolution is the ability of the scheme to capture the spatial variations associated with the detached shear layer above the separation bubble, both because of the increased wall-normal velocity gradient $\partial\overline{u}/\partial y$ and because of the thickening influence of the APG, which transports nearer-wall turbulence upwards (cf. figure 1) into regions of larger wall-normal spacing Δy (recall that with the spectral method, it is not an option to independently refine in one region or another). Consequently, Δy is the largest multiple of the local Kolmogorov length scale η here. The maximum occurs for Case C, with $\Delta y/\eta = 9.2$ (the maximum for both A and B is approximately 6.5). As this is (just) within the range required for spectral methods to produce accurate first- and second-order statistics (Moin & Mahesh 1998), we do not expect the results presented below to suffer from appreciable spatial-resolution-induced inaccuracies. (Sandham (2002) quotes a smaller critical value, $\Delta y/\eta \approx 5$, perhaps to account for lower-order, non-spectral schemes.) However, we should point out that the resolution is not fine enough to completely accommodate the small but non-zero vorticity near the top wall, at $x \approx 0$ stations, where the boundary layer is thickest, and thus yields the worst-case condition (see figures 2 and 8*b*). This deficiency (which was more pronounced in SC97) is revealed by the minor near-wall oscillations (Gibbs phenomenon) in the $x = 0$ profiles for all three cases (figure 4). While these oscillations imply that certain statistics, for example Reynolds-stress budgets, will be somewhat suspect near separation, their magnitude is a relatively small fraction of the maximum, and the oscillations evidently have negligible effect on results at other stations: note the smooth behaviour (also found

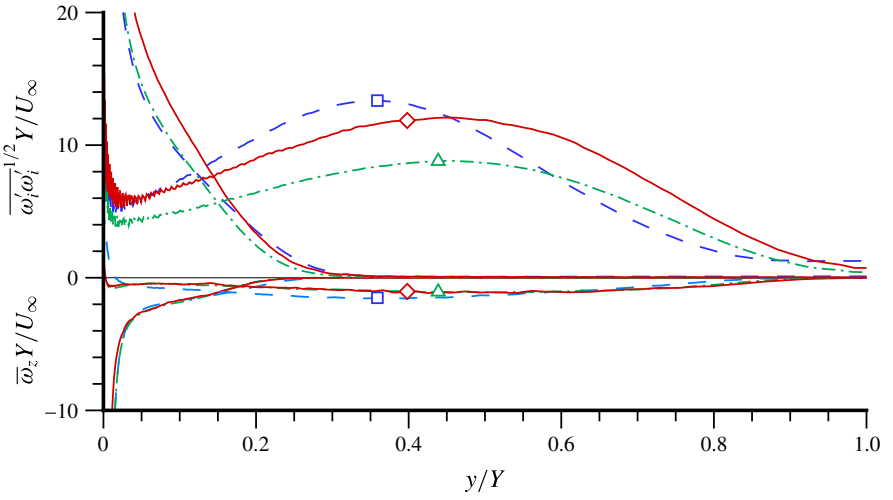

FIGURE 4. (Colour online) Profiles of mean spanwise vorticity $\overline{\omega}_z$ and root-mean-square enstrophy fluctuations $\overline{\omega_i'\omega_i'}^{1/2}$ in ZPG regions (no symbols, at x locations specified in figure 5*a*) and at $x = 0$ (symbols): - - - -/□ (blue), Case A; — · —/△ (green), Case B; ——/◇ (red), Case C.

at other stations away from $x \approx 0$) of both the fluctuation- and mean-vorticity profiles from the ZPG regions of all three cases, shown in figure 4 (no symbols), and the overall momentum balance in figure 17 (appendix C). This residual error is therefore not expected to seriously compromise any of the lower-order statistics, or the conclusions upon which they are based.

The present streamwise Λ_x and spanwise Λ_z domain sizes represent considerable improvements over those of SC97, with Λ_x and Λ_z now 2.6 and 2.8 times larger, respectively. The former allows a canonical ZPG layer to form upstream of separation, as well as significant redevelopment toward ZPG conditions downstream of reattachment; the latter avoids constraint of the large-scale structures that tend to form away from the wall, downstream of the separation region (cf. Na & Moin 1998; Abe 2017). The sufficiency of Λ_z was confirmed by inspecting two-point spanwise correlations in appropriate regions. The adequacy of the domain periods is also supported by figure 1, which presents Case A visualisations from a subregion ranging from $x = \pm 5.5Y$ (centred about $x = 0$), and spanning half the full Λ_z domain.

Each case was initialised by random velocity fluctuations that approach zero in the free-stream as $(y/Y)\exp(-0.1y^2/Y^2)$. A mixed implicit/explicit (Crank–Nicolson/Runge–Kutta) time-advance algorithm is used (Spalart *et al.* 1991), under conditions of constant peak Courant–Friedrichs–Lewy (CFL) number, of 1.7, with respect to a Galilean reference frame translating at $0.4U_\infty$ (to maximise the allowable time-step). This yields an average time-step of $\Delta t \approx 1.5 \times 10^{-3} Y/U_\infty$ for Case A, $1.7 \times 10^{-3} Y/U_\infty$ for Case B, and $9.3 \times 10^{-4} Y/U_\infty$ for Case C; the corresponding values in wall units are respectively $\Delta t^+ = \Delta t\, u_\tau^2/\nu \approx 0.15$, 0.17 and 0.155.

Statistics were gathered by averaging over z and in time, involving 1066, 1051 and 278 full x–y fields over periods of 186.5, 195 and $52Y/U_\infty$, respectively, for Cases A, B and C (respectively corresponding to 7.2, 7.5 and 2.0 domain-flow-through times Λ_x/U_∞). Some quantities were also locally averaged in x, using a Gaussian filter of width $0.02Y$ to $0.06Y$. (See figures 3*c*, 6, 7*b*, 8, 10*b*,*f*, 15, 12, 16*a* and 17*b*.) The

z- and t-averaged data are available from the NASA Turbulence Modeling Resource (TMR) website, https://turbmodels.larc.nasa.gov.

Computations were run on the NASA Advanced Supercomputing (NAS) Division's Pleiades system, a distributed-memory SGI ICE cluster, on from 1024 to 4096 cores. A total of about 94 600 (Case A), 92 700 (B) and 357 000 (C) CPU core hours were utilised during the statistics-gathering phase of the computations.

3. DNS results

The results in this section were chosen primarily because of their relevance to basic questions regarding turbulence theory and RANS modelling. After considering the quality of the ZPG flow upstream of the separation (in § 3.1), and therefore the flow's suitability as a RANS-modelling benchmark (or as the subject for DNS and LES studies by other groups), we investigate the general characteristics of the flow, via the streamwise variations of its mean and integral quantities (§ 3.2). The pressure-gradient-induced changes of the mean-velocity profiles are then examined, in terms of near-wall scaling, as the mean skin friction falls and later recovers towards ZPG conditions, and in terms of the 'Stratford scaling', as the skin friction approaches zero (§ 3.3). The streamwise evolution of the terms in the turbulent-kinetic-energy (TKE) budget is then documented for the highest-Re data (Case C) (§ 3.4), after which these results are used to determine the sensitivity to pressure gradient of algebraic near-wall length scales used by wall functions and some common RANS transport models (§ 3.5).

3.1. *ZPG reference state*

The degree to which we have met the objective of achieving a canonical ZPG state upstream of the APG, for each of the three cases, can be assessed in figures 5 and 6. The ZPG reference stations are chosen as $x/Y = -5$ for Case A, -8 for B and -9.5 for C; at these stations, the local pressure gradient in wall units, $p^+ = (\mathrm{d}P/\mathrm{d}x)(\nu/u_\tau^3)$, is 0.000 (A), 0.001 (B) and 0.000 (C). The mean-velocity and $-\overline{u'v'}$ shear-stress profiles, the displacement/momentum-thickness shape factor, and the skin friction are all characteristic of constant free-stream velocity boundary layers at their respective Reynolds numbers ($R_\theta = 1035$, 876 and 1744, for Cases A–C). The present situation is significantly better than for SC97, for which $R_\theta \approx 300$, a pronounced log-law region, was absent (figure 5a), and the skin friction was abnormally low (figure 5b). In contrast, the R_θ dependence of δ^*/θ and C_f from the new runs compares well with previous DNS (Spalart 1988) and the (Coles 1962) data for ZPG boundary layers. The Case C TKE and TKE budget in figure 6 also agree extremely well with Schlatter & Örlü's (2010) ZPG DNS at $R_\theta = 2000$. This agreement, for various quantities, provides strong evidence for the success of the fringe-zone inflow/outflow treatment, in allowing a spatially developing flow to be faithfully represented in a periodic domain, and for the adequacy of the streamwise domain size, in allowing sufficient length for the flow to develop toward a universal ZPG state defined solely by R_θ.

The solid line in figure 5(b) is a curve fit of the C_f versus R_θ relationship found in the Coles results. As mentioned above, this was used (by integrating the ZPG momentum-integral equation $\mathrm{d}\theta/\mathrm{d}x = C_f/2$) to estimate the θ variation with x of the virtual ZPG boundary layer into the APG region – and thus set the origin (i.e. location of the APG-to-FPG transition) for the transpiration profile $V_{top}(x)$ for the three cases; see figure 3(a,c). For each of Cases A, B and C, we conclude that the ZPG boundary

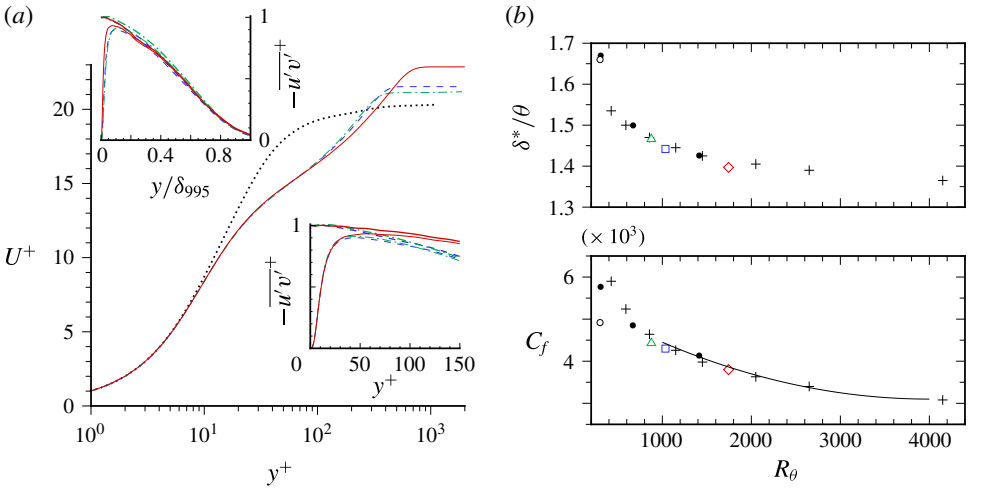

FIGURE 5. (Colour online) (*a*) Mean-velocity and $-\overline{u'v'}$ shear-stress profiles in ZPG regions: ·····, SC97; - - - - (blue), Case A ($x/Y = -5$); — · — (green), Case B ($x/Y = -8$); —— (red), Case C ($x/Y = -9.5$). Thicker lines in inset plots show $\tau/\rho = -\overline{u'v'} + \nu\,\partial\,\overline{u}/\partial y$. (*b*) Skin friction and shape factor: +, Coles (1962); ●, Spalart (1988); ○, SC97; □ (blue), Case A; △ (green), Case B; ◇ (red), Case C; ——, interpolant of Coles data for $1000 < R_\theta < 4000$: $C_f = a + bR_\theta + cR_\theta^2$, with $(a,b,c) = (0.0055, -1.2 \times 10^{-6}, 1.5 \times 10^{-10})$. Skin friction based on reference velocity, $C_f = \tau_w/(1/2)\rho U_\infty^2$. DNS thicknesses from (3.1)–(3.4).

layers to which the APG is applied is indeed canonical, in the sense that it can be uniquely specified solely in terms of its thickness (since θ defines R_θ which defines C_f which defines $\mathrm{d}\theta/\mathrm{d}x$). This is an essential feature for DNS (or experimental) data that are to be used as a benchmark for RANS-model testing. Note, however, that the Reynolds numbers considered here are still somewhat below the range RANS modellers seem to have been able to cover well when they developed their closures for ZPG boundary layers. (The minimum appears to have been $R_\theta \approx 5000$; see results presented on the TMR website (https://turbmodels.larc.nasa.gov), and recall historical estimates that 'low-Reynolds-number effects' in the ZPG flow end around $R_\theta \approx 6000$.) On the other hand, asking a RANS model to capture the skin friction at $R_\theta \approx 2000$ does not strike us as an unreasonable or irrelevant exercise. We describe below how this can be done for a one-equation eddy-viscosity scheme. Moreover, the separation phenomena of interest in this study are either controlled by essentially inviscid processes, or will have their Reynolds-number sensitivity revealed by a comparison of the SC97, A, B and C results.

3.2. *Basic features of the separation bubble*

Highlights of this subsection include Reynolds-number dependence of the skin-friction behaviour, comparison of alternative measures of the boundary-layer thicknesses, and a test of integral-parameter predictions of separation.

The geometry and general overview of the flow are illustrated above, in figures 1–3. The turbulence structures in figure 1 reveal a number of noteworthy qualitative features. The relative size of the structures points to the adequacy of the domain size. (Recall that these plots contain x–z subregions of the Case A domain, 42 % of Λ_x

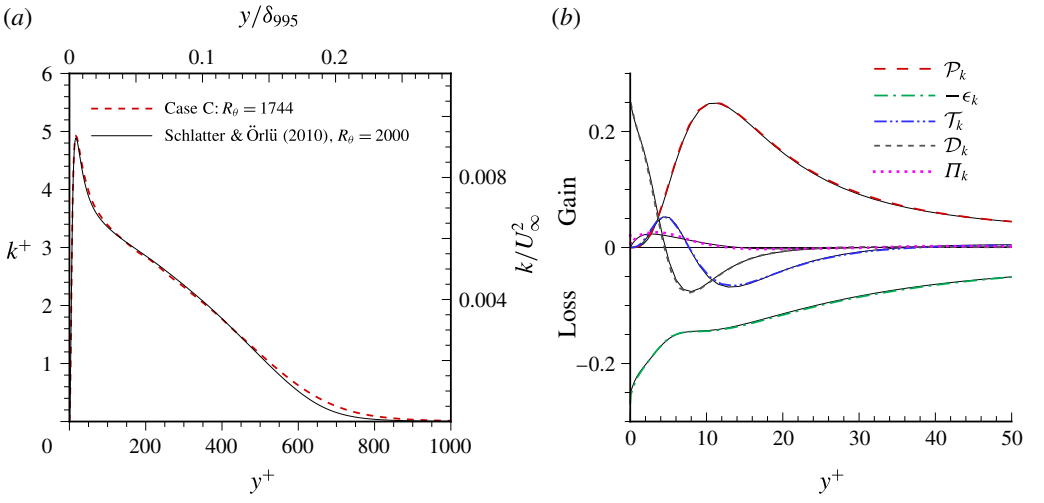

FIGURE 6. (Colour online) Profiles of (*a*) turbulent kinetic energy (TKE), $k = (1/2)\overline{u_i' u_i'}$, and (*b*) terms in TKE budget for Case C in ZPG region ($x/Y = -9.5$; $R_\theta = 1744$). Production rate, $\mathcal{P}_k = -\overline{u_i' u_j'}\partial\overline{u}_i/\partial x_j$; dissipation rate, $\epsilon_k = \nu\overline{(\partial u_i'/\partial x_j)(\partial u_i'/\partial x_j)}$; turbulent transport, $\mathcal{T}_k = -(1/2)\partial\overline{u_i' u_i' u_j'}/\partial x_j$; viscous transport, $\mathcal{D}_k = \nu\,\partial^2 k/\partial x_j \partial x_j$; velocity–pressure-gradient correlation, $\Pi_k = -\overline{(u_i'/\rho)\partial p'/\partial x_i}$. All budget terms computed directly, except Π_k, which is inferred from imbalance (including $\mathcal{D}k/\mathcal{D}t$). Budget terms normalised by u_τ^4/ν, where $u_\tau/U_\infty = 0.0436$ and $u_\tau Y/\nu = 349$. Thin solid curves in (*a*) and (*b*) are from Schlatter & Örlü's (2010) ZPG turbulent-boundary-layer DNS at $R_\theta = 2000$. Results have been locally averaged in x.

and 50 % of Λ_z.) Figure 1(*a*) shows the fully turbulent nature of the separation, and that the vortex structures, visualised by isocontours of the so-called Q-criterion (Hunt, Wray & Moin 1988), are convected away from the wall in the APG, and toward it in the FPG (these isocontours are coloured by wall-normal distance). The velocity contours in figure 1(*b*,*c*) display the increase in size, relative to those found upstream, of the turbulence structures streaming from near the reattachment station (cf. Abe *et al.* 2012; Abe 2017). (That the large-scale structures are not also found upstream of the separation is another indication of the success of the fringe inflow/outflow treatment.) The effect of the APG on the near-wall streaks – in particular how they terminate just upstream of the mean separation – can be seen in figure 1(*d*) (the red regions in this plot correspond to reversed flow, which tend to reach upstream into the low-speed 'valleys'). The streaks eventually regain their canonical/ZPG shape and spacing in the recovery region downstream of reattachment.

The grey/shaded zones in figure 2 indicate the approximately 15 % of the domain in which the fringe boundary-condition terms are active, and how they allow the non-shaded 'useful region' of the periodic domain to faithfully represent the spatial development of mean statistics. The large fraction of domain devoted to the ZPG regions upstream and downstream of the small separation bubble is apparent. (Note the mean backflow within the bubble, indicated by pink in figure 2*a*.) The significant thickening of the boundary layer, induced by the transpiration boundary conditions at $y = Y$, is evident in the mean streamlines and spanwise-vorticity contours. For all three cases, and SC97, the dividing streamline of the bubble is characterised by a near-wall 'needle' projecting upstream, while its most-downstream location

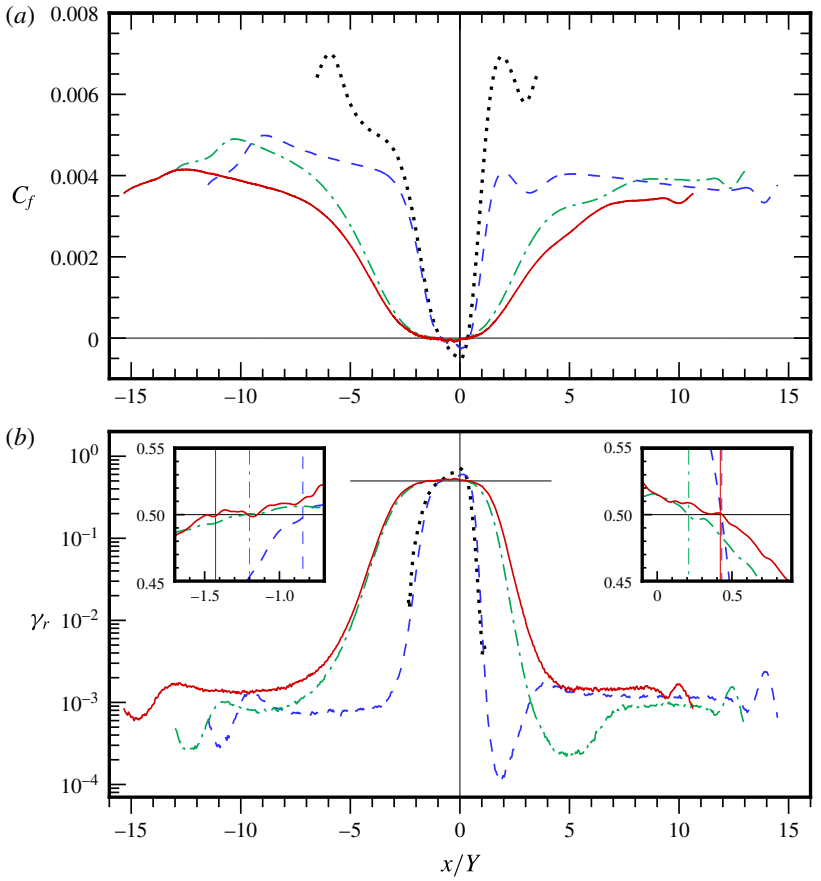

FIGURE 7. (Colour online) (*a*) Skin friction $C_f = \tau_w/(1/2)\rho U_\infty^2$ and (*b*) fraction of reversed wall shear γ_r: ·····, SC97; - - - - (blue), Case A; — · — (green), Case B; —— (red), Case C. Horizontal lines in (*b*) denote $\gamma_r = 0.50$ threshold; vertical lines in inset plots indicate $C_f = 0$ locations. The γ_r profiles in (*b*) have been locally averaged in x.

indicates a significant wall-normal velocity into the reattachment point. (For Case A, compare the $C_f = 0$ locations in figure 2, indicated by the vertical lines, with the streamline emanating from and returning to the surface.) This fore–aft asymmetry in bubble shape can also be observed, for example, in Na & Moin's (1998), Skote & Henningson's (2002) and Raiesi *et al.*'s (2011) simulations.

We have left unanswered the question of whether or not one prominent feature of many separated flows, namely a low-frequency 'breathing' oscillation (i.e. expansion and contraction) of the bubble (e.g. Castro & Haque 1987; Weiss, Mohammed-Taifour & Schwaab 2015), is present in the current configuration. The inability to consider the breathing oscillation (which differs qualitatively from the somewhat higher-frequency 'shedding' motion, associated with the roll-up of spanwise vortices in the shear layer above the bubble, found by Na & Moin (1998) and Weiss *et al.* (2015)) is a consequence of limited computational resources: since the oscillation frequency in question is apparently of the order $0.01U_\infty/L_b$, where L_b is the bubble length (Weiss *et al.* 2015), a sampling period of many multiples of $200Y/U_\infty$ would be required

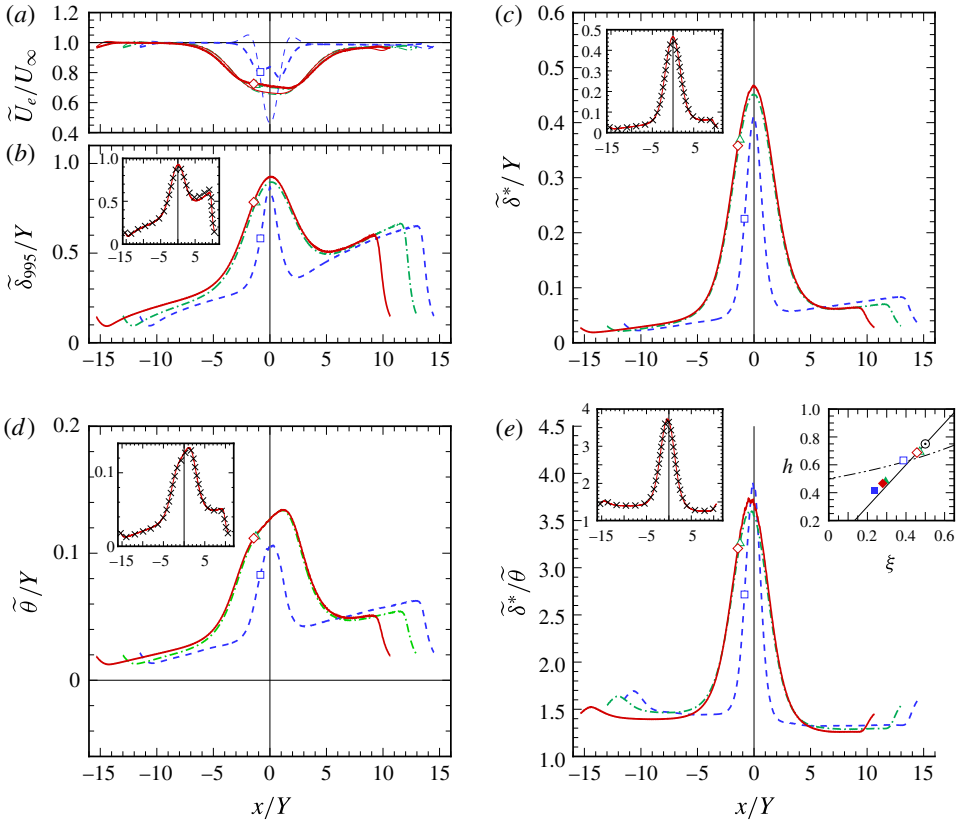

FIGURE 8. (Colour online) Edge velocities and thicknesses: - - - -/□/■ (blue), Case A; — · —/△/▲ (green), Case B; ——/◇/◆ (red), Case C. Open and closed symbols correspond respectively to full separation ($C_f = 0$) and intermittent transitory detachment ($\gamma_r = 0.2$) locations (the latter only in inset plot in *e*). Thinner curves in (*a*) are $U_{top} = \overline{u}(x, Y)$. Left-hand-side inset plots in (*b–e*) (Case C): ×, Vinuesa *et al.* (2016) thicknesses (adjusted to 99.5 % criterion), with δ^* and θ defined in terms of mean velocity integrated from $y = 0$ to the δ_{995} given by the Vinuesa *et al.* (2016) formulation. Right-hand-side inset plot in (*e*): ——, Kline, Bardina & Strawn (1983) model of high-*Re* quasi-equilibrium PG boundary layers, $h = 1.5\,\xi$; — · · —, Sandborn & Kline (1961) intermittent transitory detachment criterion, $h = 1/(2 - \xi)$; ⊙, Kline *et al.* (1983) $C_f = 0$ prediction, $(\xi, h) = (0.5, 0.75)$. Results have been locally averaged in x.

to capture it – much greater than the $187Y/U_\infty$ utilised for Case A, $195Y/U_\infty$ for Case B and especially $52Y/U_\infty$ for Case C. It should be noted, however, that the characteristics of the present DNS may *a priori* rule out any very-large-scale oscillations. Either the 'clean' (spanwise periodic) geometry (involving no upstream unsteadiness or side-wall wind-tunnel effects), the (steady) transpiration boundary condition (which is imposed relatively close to the top of the turbulent layer near its detachment) and/or the fringe treatment (which significantly reduces and 'locks in' the layer thickness at the in/outflow of the domain) may prevent the bubble length from expanding/contracting as it does in less constrained or less idealised flows.

The scope of the boundary-layer thickening is also evident in figure 3(*b*), by the significant difference between the variation of the pressure which would be

associated with $V_{top}(x)$ in the absence of a boundary layer (thinner curves) and that of the actual mean pressure at the wall, for all cases (the open symbols in this figures correspond to the mean separation and reattachment locations). The displacement (pressure-relieving) effect is such that the flow in the bubble is subject to an approximately constant APG (note the difference between the present pattern, namely strong-APG/weak-APG/strong-FPG, and the pattern of laminar separation bubbles which is essentially weak-APG/ZPG/strong-APG). This point will be revisited below, when we examine the Stratford scaling of the mean-velocity profiles in this region. Separation occurs between $C_p = 0.375$ and 0.497, with the higher value corresponding to more gradual APG, as one might expect.

Figure 7(*a*) shows the Reynolds-number *Re* dependence of the skin-friction distribution $C_f(x)$ (as well as the benefits of a larger streamwise domain, relative to that used in SC97). This dependence includes the C_f reduction with increasing *Re* in the ZPG regions, and especially the behaviour downstream of reattachment: the local minimum toward the end of the FPG (near $x/Y = 3$) appears to be purely a consequence of the rapid reversal of the pressure gradient. The local C_f maximum in the FPG between reattachment and the start of the ZPG recovery correlates with a local minimum of the fraction of reversed wall shear γ_r, before it recovers toward the small but non-zero values found in the ZPG upstream of separation. We note that this local γ_r minimum, along with the corresponding local C_f maximum, does not appear in the higher-*Re* flow, Case C. Another observation, perhaps more relevant to real-world applications, is that the percentage of reversed flow is never exactly zero in the ZPG regions, where γ_r tends to increase with Reynolds number. This behaviour (non-zero γ_r and its increase with *Re* in ZPG layers) was also observed by Spalart (1988), who attributed it to the increasing ratio between the root-mean-square fluctuations and the mean skin friction. In other words, infrequent instantaneous reversal is not always an indication of impending separation. A final observation regarding figure 7(*b*) is the very close agreement between the $C_f = 0$ and $\gamma_r = 0.50$ locations, both for separation and reattachment (inset plots).

The boundary-layer thicknesses are presented in figure 8. To accommodate the non-zero $\partial U/\partial y$ $(= \partial V/\partial x)$ in the (irrotational) free-stream of pressure-gradient layers, which defeats the definitions inherited from boundary-layer theory, we follow Lighthill (1963) and define these integral quantities in terms of a 'generalised velocity'

$$\widetilde{U}(x, y) \equiv -\int_0^y \overline{\omega}_z(x, y')\,\mathrm{d}y', \tag{3.1}$$

such that the edge (of vorticity) velocity is

$$\widetilde{U}_e(x) \equiv \widetilde{U}(x, y \to \infty), \tag{3.2}$$

and $\widetilde{\delta}_{995}$ at each x is the height at which $\widetilde{U}/\widetilde{U}_e = 0.995$. The corresponding displacement and momentum thicknesses (Spalart & Watmuff 1993) are

$$\widetilde{\delta}^*(x) \equiv \frac{-1}{\widetilde{U}_e(x)} \int_0^\infty y\,\overline{\omega}_z(x, y)\,\mathrm{d}y, \tag{3.3}$$

and

$$\widetilde{\theta}(x) \equiv \frac{-2}{[\widetilde{U}_e(x)]^2} \int_0^\infty y\,\widetilde{U}(x, y)\,\overline{\omega}_z(x, y)\,\mathrm{d}y - \widetilde{\delta}^*(x). \tag{3.4}$$

The relationship between these thicknesses and the integrated momentum balance is considered in appendix C. Note that in ZPG regions, where $\overline{\omega}_z \to -\partial\overline{u}/\partial y$, $\widetilde{U}(x, y)$ reduces to $\overline{u}(x, y)$ and these vorticity-based parameters are equivalent to the conventionally defined U_e, δ_{995}, δ^* and θ.

The difference between $\widetilde{U}_e$ given by (3.2) and the mean streamwise velocity along the top wall, $U_{top}(x) = \overline{u}(x, Y)$, is greatest for Case A (figure 8*a*). This is a consequence of its very rapid $\mathrm{d}P/\mathrm{d}x$ (i.e. more peaked transpiration profile). In fact, $\mathrm{d}V_{top}/\mathrm{d}x$ $(= \partial\overline{u}/\partial y|_{y=Y})$ is so large for this case (and for SC97) that in the irrotational region near the top wall it is associated with positive $\partial\overline{u}/\partial y$ large enough to effect a weak spurious acceleration, $\mathrm{d}U_{top}/\mathrm{d}x > 0$, in the APG region, where $\mathrm{d}P/\mathrm{d}x$ is positive along the bottom wall (figure 3*b*); compare thin- and thick-dashed lines in figure 8(*a*). The U_{top} overshoot does not occur for Cases B and C, since their transpiration profile is spread over a wider streamwise distance. Note that these deviations from boundary-layer behaviour are not an issue when testing models in a Navier–Stokes CFD code; on the other hand, some physical interpretations especially of axis-dependent quantities such as the Reynolds shear stress demand care.

The 99.5 % boundary-layer thickness profiles in figure 8(*b*), defined by $\widetilde{U}$, are essentially equivalent to those traced by the constant-$\overline{\omega}_z$ contour (not shown) that passes through $y = \widetilde{\delta}_{995}$ in the ZPG reference stations, until downstream of separation, where opposite-signed $\overline{\omega}_z$ is introduced. The location at which the conventionally defined displacement and momentum thicknesses (i.e. $\overline{u}$-based integrals from $y = 0$ to Y; also not shown in figure 8) deviate from the corresponding vorticity-based quantities corresponds to the stations beyond which the APG begins to affect the flow. These end-of-ZPG locations ($x/Y \approx -8$ for Case C) are close to those downstream of which the pressure-related terms in the momentum balance are non-negligible (cf. figure 17).

Another strategy to quantify the thickness δ of boundary layers in pressure gradients involves the relationship between the streamwise Reynolds-stress and mean-velocity profiles toward the upper edge of the layer. In light of Alfredsson, Segalini & Örlü's (2011) so-called 'diagnostic plot', modified (using the shape factor) to account for non-zero pressure gradients (Drózdz, Elsner & Drobniak 2015), Vinuesa *et al.* (2016) appeal to the apparent universal dependence of $(\sqrt{\overline{u'u'}}/(\overline{u}\sqrt{\delta^*/\theta})$ upon $\overline{u}/U_{ref}$ as $\overline{u}$ approaches U_{ref} from below, where the reference velocity U_{ref} (equivalent to the free-stream velocity in ZPG layers) is the mean value just above the edge of the turbulent layer. (Except at stations where the $\overline{\omega}_z$ profile is of two signs, U_{ref} turns out to be nearly the same as $\widetilde{U}_e$.) This dependence implicitly defines the boundary-layer thickness and U_{ref}, both of which, along with the displacement and momentum thicknesses, can be computed via an iterative calculation. The 99.5 % and integral thicknesses resulting from applying this procedure to the Case C statistics are shown by the cross symbols in the inset plots in figure 8(*b–e*). The good agreement with the vorticity-based thicknesses (3.1)–(3.4) is surprising and striking – especially since the diagnostic-plot relationship has no known physical basis (Castro 2015).

The shape factor $H = \widetilde{\delta}^*/\widetilde{\theta}$ associated with separation for the three cases ranges from 2.7 to 3.25 (figure 8*e*). In some theories and calculation methods, H_{sep} is used as a simple indicator. This is larger than the $1.8 \leqslant H_{sep} \leqslant 2.4$ cited by Cebeci & Bradshaw (1977) but smaller than the $H_{sep} = 4$ proposed by Kline *et al.* (1983). The right-hand-side inset plot in figure 8(*e*) presents the Kline *et al.* model in terms of $h = (H-1)/H$ (which lies between 0 and 1) and the displacement/boundary-layer thickness ratio $\xi = \delta^*/\delta_{995}$; the closed and open symbols in this plot respectively correspond to Simpson's

(1980) 'intermittent transitory detachment' (defined as the $\gamma_r = 0.2$ location) – referred to as 'incipient detachment' by Kline *et al.* (1983) – and full separation ($C_f = 0$) from the three DNS solutions (in terms of $\widetilde{\delta}_{995}$, $\widetilde{\delta}^*$ and $\widetilde{\theta}$). The DNS results are fairly close to Kline *et al.*'s (1983) quasi-equilibrium model of attached and detached pressure-gradient (PG) boundary layers (based on Cole's (1956) classical log-law/wake structure, modified to account for $u_\tau^2 \leqslant 0$ (see Kline *et al.*), and used to construct their separation correlation), which at high Reynolds number is well approximated by $h = 1.5\,\xi$ (solid line). On the other hand, the DNS is well below the Kline *et al.* prediction of full separation and especially intermittent transitory detachment, given respectively by the $H_{sep} = 4$ location mentioned above, at $\xi_{sep} = 0.5$ and $h_{sep} = 0.75$ (circle-dot symbol), and by the intersection of the general quasi-equilibrium boundary-layer line with the chain-double-dot curve (cf. Simpson 1989; Cheng *et al.* 2015). We thus find that, in general, neither a critical C_p (recall figure 3*b*) nor an integral/shape-factor threshold provide a particularly precise parameterisation of separation for the present cases.

3.3. *Mean-velocity profile evolution*

The theme of this subsection is the search for – and deviation from – near-wall similarity of the mean velocity in regions with non-zero pressure gradient, for stations with both finite and zero mean skin friction.

The effect of the APG on the mean velocity in inner/wall units is shown in figure 9. The velocity gradient $\partial U/\partial y$ outside the turbulent region is apparent. The present results do not support the proposal that the ZPG log law will survive when the maximum shear stress is less than 1.5 times the wall value (see stress profiles in inset plots), or when the magnitude of p^+ is less than 0.050 (denoted by + symbols in figure 9*a–c*); see for example Simpson (1989) and Driver (1991). The deviation from the (nominally) logarithmic ZPG profile depends upon the Reynolds number and even more on the strength/duration of the APG. The controlling influence of the pressure gradient is revealed by its effect upon the $-\overline{u'v'}$ shear stress. The abrupt deceleration imposed for Case A has little impact upon the shape of the $-\overline{u'v'}$ profile (typical of ZPG conditions; see upper-left inset in figure 9*a*), since the wall shear-stress reduction for this case has too little time to diffuse into the outer-layer turbulence (and the magnitude and duration of the outer-layer $\partial\overline{v}/\partial y$ strain are too small to effect significant $-\overline{u'v'}$ production; cf. Coleman, Kim & Spalart 2003) before the mean skin friction changes sign, relative to the less-sudden APGs of Cases B and C; contrast the fuller $-\overline{u'v'}$ versus y/δ_{995} profiles in figure 9(*b*,*c*). These shear-stress changes are accompanied by departures from the log profile of the mean velocity that are quite general (rather than progressive; cf. Galbraith *et al.* 1977), roughly beginning at a given y^+ for each case, rather than a given y/δ, plausibly correlated with the different values of p^+. A visual inspection of these profiles could lead to the interpretation that they still contain a logarithmic layer, but one with lower value of the von Kármán constant κ. We resist such interpretations, not having any evidence of these putative log layers lengthening with Reynolds number the way they do in ZPG. This is a reminder of the difficulty in defining equivalent flows at different Reynolds numbers when strong pressure gradients are at play. (Skote & Henningson (2002) advocate an alternative perspective, and propose a log-law profile for both attached and separated cases.)

The common practice of mapping the magnitude of U^+ at $y^+ = 50$ versus p^+ to quantify PG-induced deviations from the log law (see for example Johnstone *et al.*

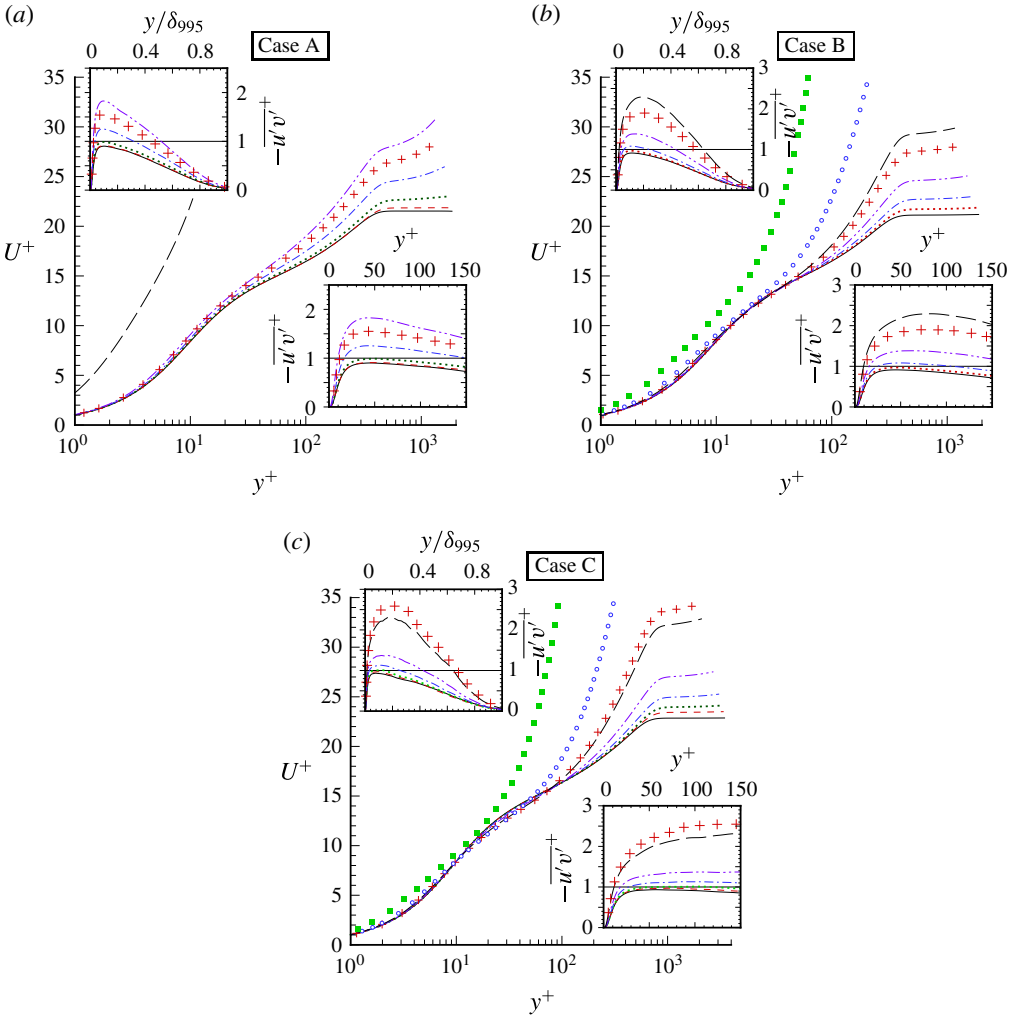

FIGURE 9. (Colour online) Mean-velocity profiles before separation, for $y \leqslant Y$. (*a*) Case A: —— (dark), $x/Y = -5(p^+ = 0.000)$; - - - - (red), $x/Y = -4(p^+ = 0.000)$; · · · · · · (green), $x/Y = -3(p^+ = 0.006)$; — · — (blue), $x/Y = -2.4(p^+ = 0.026)$; + (red), $x/Y = -2.14(p^+ = 0.050)$; — · · — (violet), $x/Y = -2(p^+ = 0.070)$; – – – – (dark), $x/Y = -1(p^+ = 0.749)$. (*b*) Case B: —— (dark), $x/Y = -8(p^+ = 0.001)$; · · · · · · (red), $x/Y = -7(p^+ = 0.004)$; — · — (blue), $x/Y = -6(p^+ = 0.010)$; — · · — (violet), $x/Y = -5(p^+ = 0.026)$; + (red), $x/Y = -4.28(p^+ = 0.050)$; – – – – (dark), $x/Y = -4(p^+ = 0.065)$; ○ (blue), $x/Y = -3(p^+ = 0.211)$; ■ (green), $x/Y = -2(p^+ = 1.132)$. (*c*) Case C: —— (dark), $x/Y = -9.5(p^+ = 0.000)$; - - - - (red), $x/Y = -8(p^+ = 0.001)$; · · · · · · (green), $x/Y = -7(p^+ = 0.003)$; — · — (blue), $x/Y = -6(p^+ = 0.008)$; — · · — (violet), $x/Y = -5(p^+ = 0.017)$; – – – – (dark), $x/Y = -4(p^+ = 0.043)$; + (red), $x/Y = -3.84(p^+ = 0.050)$; ○ (blue), $x/Y = -3(p^+ = 0.141)$; ■ (green), $x/Y = -2(p^+ = 0.825)$. Inset plots in (*a–c*) contain $-\overline{u'v'}$ shear-stress profiles, normalised by local $u_\tau^2 = \tau_w/\rho = \nu\,(\partial\overline{u}/\partial y)_{y=0}$.

2010) is nowadays complicated by the emerging consensus that a purely logarithmic profile should not be expected, if at all, below y^+ of a few hundred – Marusic *et al.* (2013) propose $y^+ = 3\sqrt{u_\tau \delta/\nu}$ as the minimum, which is about 80 at the ZPG

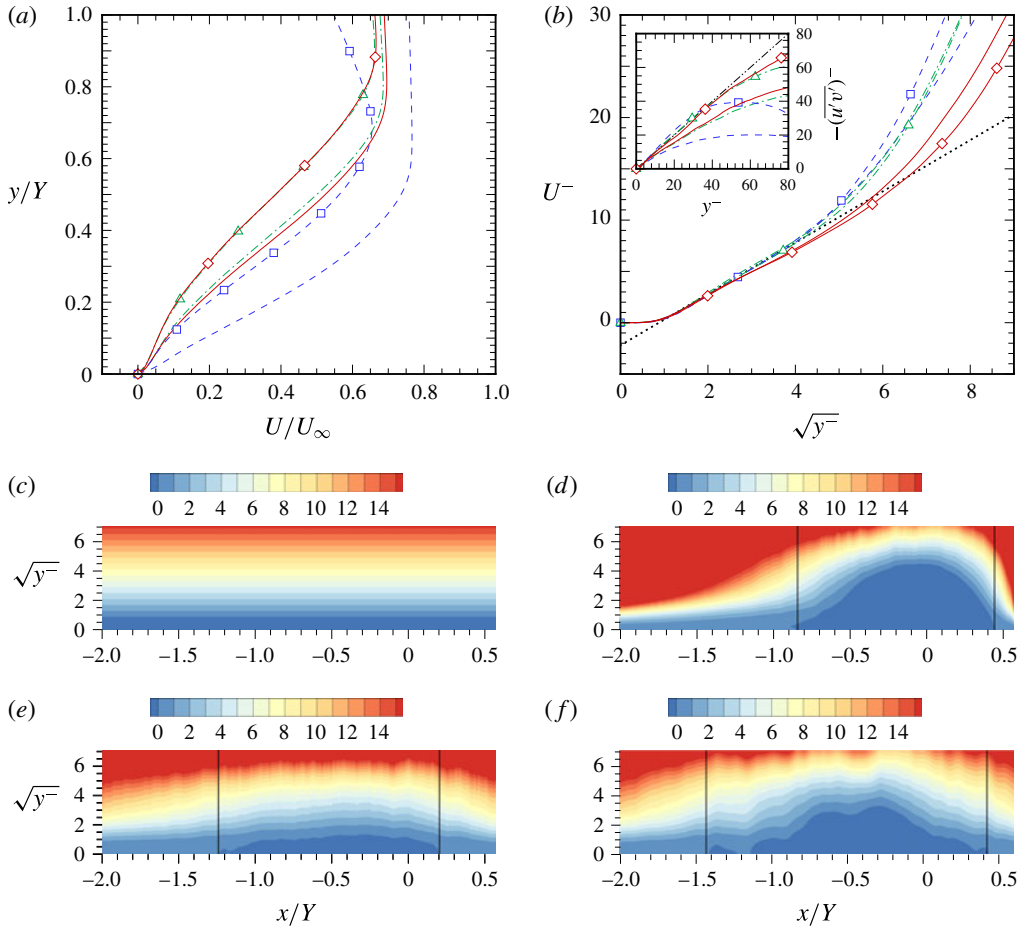

FIGURE 10. (*a*,*b*) Mean-velocity profiles at (no symbols) separation and (symbols) reattachment, (*a*) with respect to U_∞ and Y, and (*b*) in Stratford scaling: - - - - (blue), Case A; — · — (green), Case B; —— (red), Case C; · · · · · · (in *b*), Stratford's (1959) square-root-law $U^- = B\sqrt{y^-} + C$, with $(B, C) = (2.5, -2.2)$ (Coleman *et al.* 2017), where $U^- = U/u_p$, $y^- = yu_p/\nu$ and $u_p^3 = \nu \mathrm{d}(\overline{p}_{wall}/\rho)/\mathrm{d}x$. Inset plot in (*b*) contains $-(\overline{u'v'})^- = -\overline{u'v'}/u_p^2$ profiles: — · · — (dark), $-(\overline{u'v'})^- = y^-$ idealisation. (*c*–*f*) Contours of (*c*) $B\sqrt{y^-} + C$, and local U^- for Cases (*d*) A, (*e*) B and (*f*) C. Dark solid vertical lines in (*d*–*f*) indicate mean separation and reattachment stations. The Case C results have been locally averaged in x.

reference station for Case C – to say nothing about the current uncertainty in the value of κ, or the debate about its universality. We note that for Case C, opposite impressions are given by the behaviour of U^+ at $y^+ = 50$ and at $y^+ = 100$, initially decreasing for the former and increasing for the latter. Despite these complications, we shall see below that the log law tends to be at least as insensitive to pressure gradients as other near-wall quantities such as the mixing length or eddy viscosity.

Figure 10 displays velocity profiles in the separated region, specifically at separation and reattachment, for comparison with the scaling postulated by Stratford (1959) (cf. Skote & Henningson 2002). From figure 10(*a*) we find that the profiles at the

two points with zero mean skin friction do not have a universal shape when plotted versus y/Y. A figure versus y/δ would bring them closer, but still, some have an inflection point and others do not. In contrast, when drawn in 'Stratford units' y^- and U^- (see figure 10 legend), the six profiles essentially collapse up to $y^- \approx 16$, and follow the square-root law beginning around $y^- \approx 2$. (Refer to Coleman *et al.* (2017) for a discussion of why the y^- values are not very large, compared with values in the hundreds for the logarithmic law.) This is in spite of the fact that the $-\overline{u'v'}$ profiles at $C_f = 0$ are not particularly close to the linear idealisation associated with the Stratford conditions, although they are closer at reattachment (symbols) than at separation (see inset plot in figure 10*b*).

Perhaps the most significant attribute of the collapse observed for the mean velocity is that it is so well approximated by the square-root law with slope and intercept coefficients taken from an independent DNS study in Couette–Poiseuille flow (using a channel-flow code; Coleman *et al.* 2017). That flow has streamwise invariant statistics and sustained zero skin friction in the x direction, in contrast with the present one, and was deemed to give Stratford scaling and square-root behaviour a possibly atypical chance of success (Stratford's flow was different still, with sustained zero skin friction but rapid boundary-layer growth in x). The scaling appears to be very robust, the flow being dominated by the pressure gradient, which is the foundation of the Stratford units in the absence of a friction velocity. Figure 10(*d–f*) display contours of U^- in $(x, \sqrt{y^-})$ axes, to compare with contours of the square-root law shown in figure 10(*c*). They show that between separation and reattachment – where due to the displacement effect, $\mathrm{d}P/\mathrm{d}x$ is approximately constant (see figure 3*b*) – even though the negative skin friction is not strong, the quantity U^- deviates appreciably from the square-root law, especially in Cases A and C. Thus, the law is valid strictly only at two locations. Here as in the Couette–Poiseuille flow, we view this as a notable success of turbulence theory.

The weakness of the backflow magnitude – for example, for Case C, at $x/Y = -0.5$ the minimum $\overline{u}$ is $-0.004U_\infty$ – is revealed by the fact that the near-wall mean-velocity profiles in local wall units deviate from the linear $U^+ = y^+$ asymptote very close to the wall, below $y^+ = 0.5$ (cf. the corresponding profiles in figure 10 of Dianat & Castro 1989, for a more-deeply separated case). Nevertheless, the present reverse-flow profiles (not shown) are all reasonably well approximated by the expression proposed by Simpson (1983), $U/U_N = A[y/N - \ln(y/N) - 1] - 1$ (where U_N is the magnitude of the maximum negative velocity and N the distance from the wall at which it is found), provided $A \approx 0.9$ rather than Simpson's original $A = 0.3$, or the $A = 0.235$ found by Dianat & Castro (1989) to best fit their results (see also Dianat & Castro 1991). The implications of this rather large variation for A regarding the validity and universality of the U_N scaling are at present not clear.

The recovery toward the ZPG state downstream of the bubble is documented in figure 11, in terms of the mean velocity in local wall units. The present results differ from those found by Castro & Epik (1998) downstream of their separation bubble, in that rather than a monotonic approach from below, here there is an overshoot in the log law for all three cases before the ZPG profile is recovered (cf. Mohammed-Taifour 2017). (The shaded curves in figure 11*a–c* are from the ZPG reference station, upstream of the bubble; figure 5*a*.) The source of this difference is likely to be that in the Castro & Epik experiment the recovering (or more accurately, developing) turbulent layer is initiated by a transitioning laminar separation bubble, in contrast to the APG/FPG-induced turbulent separation of a well-developed ZPG layer considered here. On the other hand, the DNS and the Castro & Epik experiment

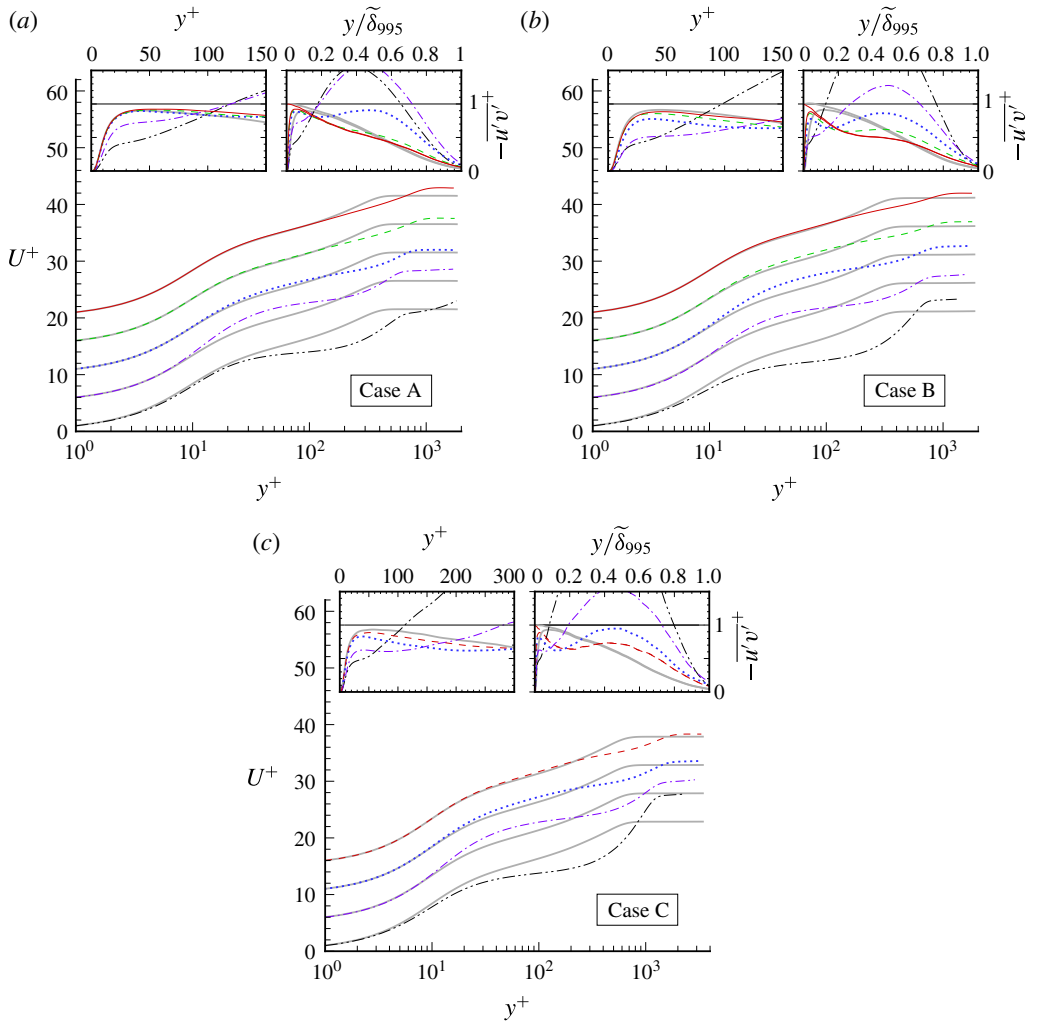

FIGURE 11. (Colour online) Mean-velocity profiles after reattachment, for $y \leqslant Y$. (*a*) Case A: — · · — (dark), $x/Y = 2(p^+ = -0.029)$; — · — (purple), $x/Y = 3(p^+ = -0.006)$; · · · · · · (blue), $x/Y = 5(p^+ = 0.000)$; - - - - (green), $x/Y = 9(p^+ = 0.000)$; —— (red), $x/Y = 11(p^+ = 0.000; R_\theta = 2360)$; —— (grey/shaded), $x/Y = -5$ $(p^+ = 0.000$; cf. figure 9*a*). (*b*) Case B: — · · — (dark), $x/Y = 3(p^+ = -0.039)$; — · — (purple), $x/Y = 5(p^+ = -0.019)$; · · · · · · (blue), $x/Y = 7(p^+ = -0.004)$; - - - - (green), $x/Y = 9(p^+ = -0.001)$; —— (red), $x/Y = 11(p^+ = -0.001; R_\theta = 2145)$; —— (grey/shaded), $x/Y = -8$ $(p^+ = 0.001$; cf. figure 9*b*). (*c*) Case C: — · · — (dark), $x/Y = 3(p^+ = -0.031)$; — · — (purple), $x/Y = 5(p^+ = -0.013)$; · · · · · · (blue), $x/Y = 7(p^+ = -0.0025)$; - - - - (red), $x/Y = 8.65(p^+ = -0.001; R_\theta = 4040)$; —— (grey/shaded), $x/Y = -9.5$ $(p^+ = 0.000$; cf. figure 9*c*). Profiles in (*a–c*) have been shifted five units in vertical scale above the one upstream, plotted below it. Inset plots in (*a–c*) contain $-\overline{u'v'}$ shear-stress profiles; total stress $\tau/\rho = -\overline{u'v'} + \nu\,\partial\,\overline{u}/\partial y$ also shown in right-hand-side subplots, for ZPG-reference and furthest-downstream stations (only).

are similar in that the inner/logarithmic (but not the outer/wake) region of a ZPG is recovered about $10\delta_r$ downstream of reattachment, where δ_r is the layer thickness at reattachment. The solid lines in figure 11(*a*,*b*), and the dashed lines in figure 11(*c*) (i.e.

the last stations unaffected by the outflow fringe for each case) correspond respectively to $(x - x_r)/\delta_r = 11.5$ (A), 9.8 (B) and 9.1 (C), where x_r is the reattachment location (equal to $0.43Y$ for A, $0.21Y$ for B and $0.42Y$ for C), and δ_r is taken as $\widetilde{\delta}_{995}$ at $x = x_r$ (see figure 8*b*). Another common feature of the experiment and the DNS is the very slow development of the outer region of the mean velocity: the outer-layer Clauser parameter $G = (2/C_f)^{1/2}(H - 1)/H$ at the furthest downstream ZPG stations ($x/Y = 12.5$, 11 and 8.65, respectively, for Cases A, B and C) is $G = 5.85$, 5.2 and 5.0 – all well below the ZPG value of 6.8 found by Coles (1962). Castro & Epik observed $G = 5.9$ at their farthest-downstream measuring station. They also found that $-\overline{u'v'}/u_\tau^2$ recovers even more slowly than the outer-layer U^+ does, and that it tends to first settle to a level lower than the pure ZPG profile at comparable Reynolds number, before it rises very slowly toward the latter. Comparable behaviour is seen here, in that $-\overline{u'v'}/u_\tau^2$ at a given y/δ_{995} is significantly less at the final prefringe locations than at the reference ZPG station from upstream (indicated in figure 11 by the solid grey/shaded curves); see for example the pronounced 'divot' relative to the ZPG profile in the Case B stress below $y/\delta_{995} \approx 0.5$, in the right-hand-side subplot in figure 11(*b*). We conclude that in none of the three DNS cases does the layer reach the canonical, fully ZPG, state before it leaves the domain. The eventual development of a standard ZPG layer well upstream of the bubble, from the distorted/recovering turbulence, is another reminder of the success of the fringe treatment.

3.4. *TKE budget*

In addition to information about the downstream development of the individual terms in the TKE budget, which is offered as an aid to modellers attempting to replicate this flow, the following results underline the importance of exercising care when transferring concepts and intuition developed in thin shear layers to flows with streamline divergence/convergence, even when it is relatively mild.

For all three cases, a local TKE maximum (in addition to the near-wall peak in the ZPG layer) occurs in the region above the upstream portion of the mean separation bubble. For Case C, the peak (which is nearly the same magnitude, in units of U_∞^2, as the near-wall ZPG-reference value; cf. figure 6*a*) is directly above the mean separation location, $x/Y = -1.43$ (figure 12*a*). This is in contrast to turbulent separation induced by surface curvature, such as in the rounded-step flow studied by Bentaleb, Lardeau & Leschziner (2012), where the TKE peak is larger (with respect to U_∞^2) and further downstream. The TKE growth or decay along mean streamlines – and thus this local maximum – is largely controlled by the imbalance between the production $\mathcal{P}_k$, dissipation ϵ_k and turbulent transport $\mathcal{T}_k$ terms. The velocity–pressure-gradient correlation Π_k is quite small except adjacent to the wall, where it acts as a source (cf. figure 6*b*). (Recall however that the pressure term acts as a strong sink for the Reynolds shear stress $-\overline{u'v'}$ across the layer (Spalart 1988).) Our focus here will be upon outer-layer regions.

The turbulent transport $\mathcal{T}_k$ (figure 12*e*) tends to spread TKE down the TKE gradients, both toward and away from the wall. It makes a particularly important contribution toward the outer edge of the turbulent layer, accounting for nearly all of the positive $\mathcal{D}k/\mathcal{D}t$ in the APG and especially FPG regions.

The evolution of the production term correlates with that of the x-component normal Reynolds stress $\overline{u'u'}$. For example, in the $\partial\overline{u}/\partial x = \mathcal{S}_{11} < 0$ (APG) region, $\mathcal{P}_k$ $(= -(\overline{u'u'} - \overline{v'v'})\,\mathcal{S}_{11} - 2\overline{u'v'}\,\mathcal{S}_{12})$ grows as $\overline{u'u'}$ does, and conversely in the FPG region. The $\overline{u'u'}$ component also contributes to a reduction in the $-\overline{u'v'}$ stress,

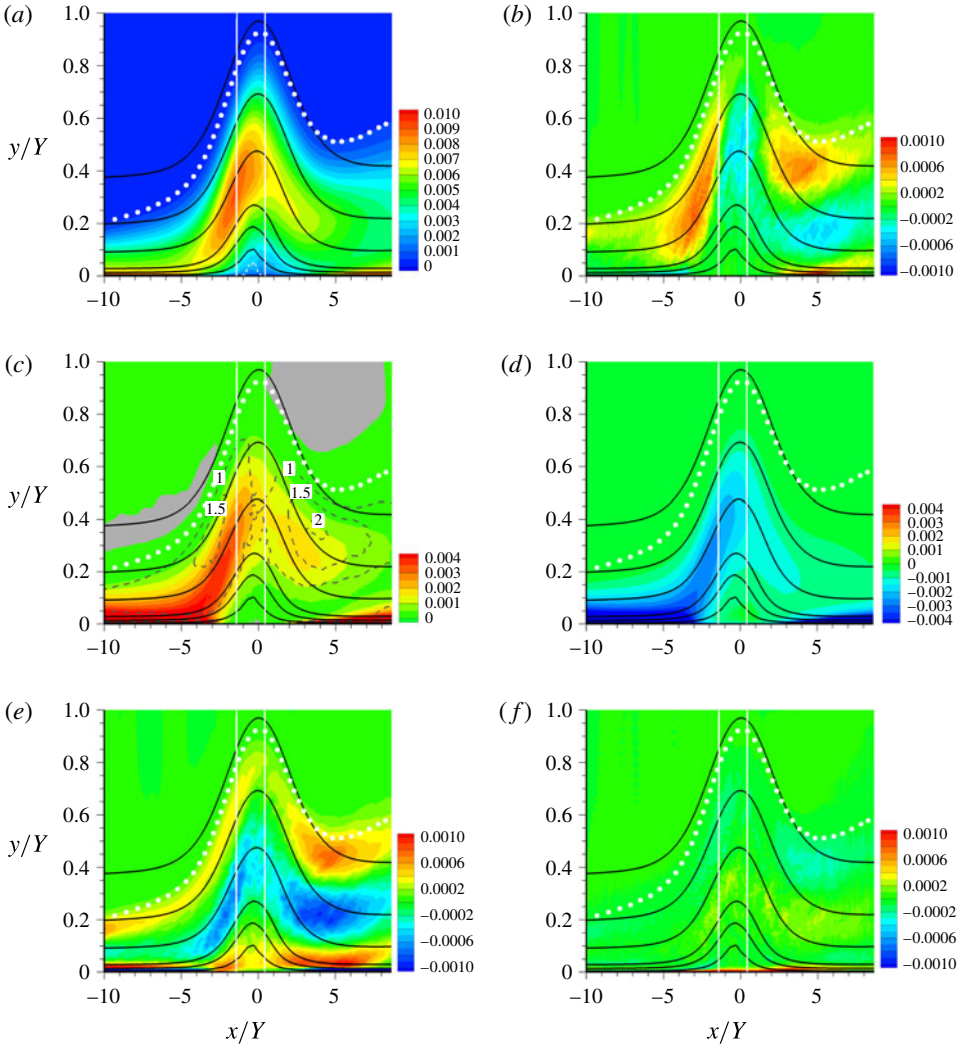

FIGURE 12. TKE budget for Case C: (*a*) TKE, $k = (1/2)\overline{u_i'u_i'}$; (*b*) $\mathcal{D}k/\mathcal{D}t = \overline{u}\,\partial k/\partial x + \overline{v}\,\partial k/\partial y$; (*c*) production rate, $\mathcal{P}_k = -\overline{u_i'u_j'}\partial\overline{u}_i/\partial x_j$; (*d*) (minus) dissipation rate, $-\epsilon_k = -\nu\overline{(\partial u_i'/\partial x_j)(\partial u_i'\partial x_j)}$; (*e*) turbulent transport, $\mathcal{T}_k = -(1/2)\partial\overline{u_i'u_i'u_j'}/\partial x_j$; (*f*) velocity–pressure-gradient correlation, $\Pi_k = -\overline{(u_i'/\rho)\partial p'/\partial x_i}$. (In ZPG regions, extrema for $\mathcal{P}_k$, $-\epsilon_k$ and Π_k, which lie outside the limits shown here, are located very near the wall; cf. figure 6, and note that at $x/Y = -9.5$, $y^+ = 50$ corresponds to $y/Y = 0.014$.) Black curves are mean streamlines; solid white vertical lines indicate mean separation and reattachment stations. White symbols denote 99.5 %-boundary-layer thickness $\widetilde{\delta}_{995}$. Broken white curve in (*a*) is mean dividing streamline of separation bubble. Broken lines in (*c*) trace contours of $\mathcal{P}_k/\epsilon_k = 1$, 1.5 and 2, while grey/shaded regions in (*c*) correspond to $\mathcal{P}_k < 0$ (minimum value is -7×10^{-5}). All terms computed directly, except Π_k, which is inferred from budget imbalance. TKE and budget terms respectively normalised by U_∞^2 and U_∞^3/Y. Results have been locally averaged in x.

through the latter's production, $-P_{12} = \overline{u'u'}\,\partial\overline{v}/\partial x + \overline{v'v'}\,\partial\overline{u}/\partial y$, coupled with the present transpiration profile, with its negative $\mathrm{d}V_{top}/\mathrm{d}x$ (figure 3*a*). For Case A, with its sudden APG/FPG, $|\partial\overline{v}/\partial x|$ is large enough to produce negative $-\overline{u'v'}$ in the outer layer, which significantly reduces the TKE production there, via the $-2\overline{u'v'}\,S_{12}$ term. In SC97, Skote & Henningson (2002) and Abe *et al.* (2012) (but not for Case A), this suppression was strong enough to yield a pocket of negative $\mathcal{P}_k$ in the outer layer, above the separation bubble. (The negative $\mathcal{P}_k$ in the free-stream, above $y = \widetilde{\delta}_{995}$, seen in figure 12*c* is statistically insignificant.) For Cases B and C, with their more gradual pressure gradients, $-\overline{u'v'}$ is everywhere positive, and the $-\overline{u'v'} < 0$ excursion of $\mathcal{P}_k$ does not occur (cf. figure 12*c*).

From the above, we see that the mean x-wise compression/expansion S_{11} provides a direct/explicit contribution to $\mathcal{D}k/\mathcal{D}t$, through the presence of this strain component in $\mathcal{P}_k$. However, we are not considering a thin shear flow exactly aligned with the x axis. This explicit dependence of the TKE production on the mean strain is more naturally viewed in terms of the compression/expansion $S^*_{11} = -S^*_{22}$ relative to Cartesian axes $(x^*_1, x^*_2) = (x_*, y_*)$ aligned with the local mean-velocity vector $(\overline{u}_1, \overline{u}_2) = (\overline{u}, \overline{v})$, with $\mathcal{P}_k$ rewritten as $= -(\overline{u'_*u'_*} - \overline{v'_*v'_*})\,S^*_{11} - 2\overline{u'_*v'_*}\,S^*_{12}$. (In these 'starred', local stream(line)-wise coordinates, we have for example, that the streamwise rate of strain is $S^*_{11} = (\overline{u}\,\overline{u}S_{11} + 2\overline{u}\,\overline{v}S_{12} + \overline{v}\,\overline{v}S_{22})/(\overline{u}\,\overline{u} + \overline{v}\,\overline{v})$ (recall $S^*_{ij} = L_{ip}L_{jq}S_{pq}$, where L_{ij} is the cosine of the angle between the x^*_i and x_j axes), and the cross-stream x^*_1–x^*_2 Reynolds shear stress is $-\overline{u'_*v'_*} = -((\overline{u}\,\overline{u} - \overline{v}\,\overline{v})\overline{u'v'} - \overline{u}\,\overline{v}(\overline{u'u'} - \overline{v'v'}))/(\overline{u}\,\overline{u} + \overline{v}\,\overline{v})$.) The shear stresses referred to the two sets of axes are appreciably different even though the streamline inclination is only of the order of 0.125 radians: compare figures 13(*c*) and 13(*e*).

In view of the large changes effected by $\mathrm{d}P/\mathrm{d}x$, it is somewhat surprising that the magnitude of the 'extra' strain S^*_{11} ('extra' in the sense of being in addition to the primary/cross-stream shear component S^*_{12}; Bradshaw 1988) that it induces is such a small fraction of the total (compare figures 13*b* with 13*a* and 13*d*). The major influence of S^*_{11} is more indirect, as we shall now see. (The magnitude of the streamline curvature, $\partial\overline{v}_*/\partial x_*$ $(= (\overline{\omega}_z + 2S^*_{12})/2)$, which is another of Bradshaw's extra strains, is even smaller than $|S^*_{11}|$ – to the point $\partial\overline{v}_*/\partial x_*$ would not register when plotted using the contour levels employed in figure 13*b*. Evidently, although the streamline inclination is not negligible – recall the large differences between $-\overline{u'v'}$ and $-\overline{u'_*v'_*}$ observed above – its variation with x is rather weak.)

An example of an indirect effect of S^*_{11} is provided by the behaviour of the $-2\overline{u'_*v'_*}S^*_{12}$ contribution to $\mathcal{P}_k$. From figure 13(*c*,*d*) we find a tendency for the streamwise increases associated with the two local maxima of the cross-stream stress $-\overline{u'_*v'_*}$ to offset the general streamwise decrease of S^*_{12}, such that their combination to $\mathcal{P}_k$ produces a net decrease that is weaker than the streamwise evolution of S^*_{12} alone would imply. Concerning the latter, since the magnitude of S^*_{12} is quite close to that of the streamwise vorticity $\overline{\omega}_z$ (not shown), which points to the dominance of the cross-stream gradient of the mean streamwise velocity $\partial\overline{u}_*/\partial y_*$, the decrease in S^*_{12} can be associated with the viscous and especially turbulent diffusion terms in the $\overline{\omega}_z$ transport equation. These diffusion terms can be interpreted as further indirect effects of the $S^*_{11} = -S^*_{22}$ straining. As initially noted by Bradshaw (1988), these types of indirect extra-strain effects are of greater importance than one might deduce from information such as that shown in figure 13(*b*).

Regarding the rate-of-dissipation ϵ_k, the third of the major terms in the outer-layer balance, we note the tendency for it to mitigate the production, with $\mathcal{P}_k/\epsilon_k$ of order one throughout the bulk of the layer (see broken-line contours in figure 12*c*). On the other hand, the dissipation is observed to follow the mean streamlines (i.e. satisfy

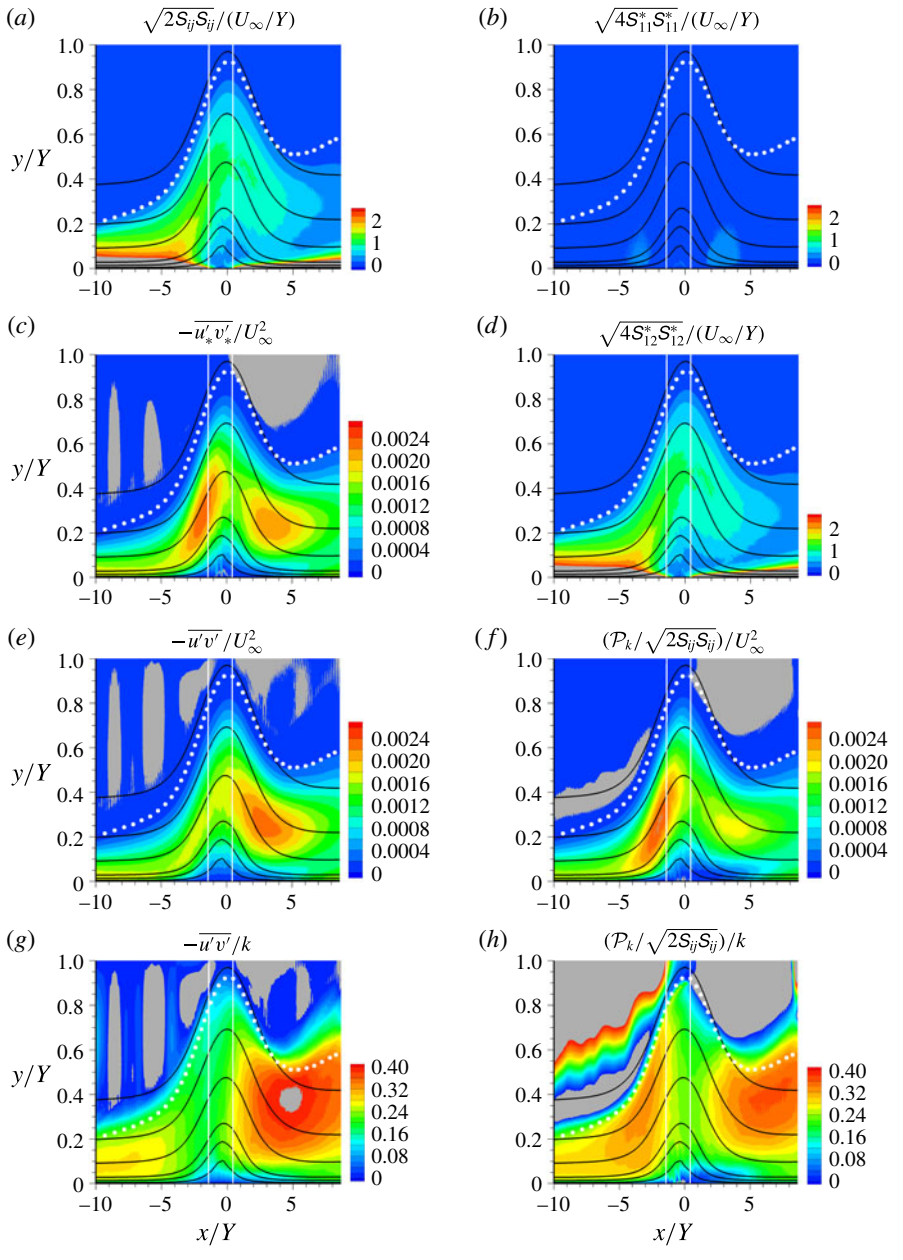

FIGURE 13. Case C contours of mean (*a*) strain rate $\sqrt{2S_{ij}S_{ij}}$, (*b*) stream(line)wise strain rate $\sqrt{4S^*_{11}S^*_{11}}$, (*c*) cross-stream Reynolds shear stress $-\overline{u'_*v'_*}$, (*d*) cross-stream strain rate $\sqrt{4S^*_{12}S^*_{12}}$, (*e*) Reynolds shear stress $-\overline{u'v'}$, (*f*) productive shear stress $-\overline{u'v'}_{prod} = \mathcal{P}_k/\sqrt{2S_{ij}S_{ij}}$, (*g*) turbulence stress–energy ratio $-\overline{u'v'}/k$ and (*h*) turbulence-to-mean energy transfer efficiency $a_{1,prod} = (\mathcal{P}_k/\sqrt{2S_{ij}S_{ij}})/k$. Quantities with '$*$' super- or subscripts are defined with respect to local Cartesian coordinates (x^*_1, x^*_2), aligned with (x^*_1) and normal to (x^*_2) mean streamlines (solid black curves). Solid white vertical lines mark mean separation and reattachment stations. White symbols denote 99.5 %-boundary-layer thickness $\widetilde{\delta}_{995}$. Grey regions indicate values outside the colour bar range shown for each figure.

$\mathcal{D}\epsilon_k/\mathcal{D}t \approx 0$) better than production does, especially downstream of reattachment (compare the $\mathcal{P}_k/\epsilon_k$ and $\mathcal{P}_k$ contours in figure 12*c*). This is not unexpected, ϵ_k being dominated by the small scales of the turbulence and not directly impacted by the pressure field. Accounting for this 'drift' of $\mathcal{P}_k$ across the streamlines into the FPG outer layer, which is consistent with the rise of $\mathcal{P}_k/\epsilon_k$ for $x > 0$, the present behaviour aligns with the standard/Kolmogorov view of the energy cascade, in that $\mathcal{P}_k < \epsilon_k$ begins to fall along mean streamlines within the APG, just downstream of the peak-TKE location – indicating the rate of dissipation is not immediately affected by the reduced TKE at larger scales (cf. Abe *et al.* 2012).

Although it is convenient to consider the Reynolds stresses and TKE budget with regard to the x–y, wall-parallel/wall-normal, coordinate system, this can produce a partial and thus misleading picture, especially in regions far from the wall, where streamline slope is not negligible, and even the streamline direction does not necessarily give a rigorous 'most relevant' set of axes. We have already observed the example provided by the significant differences between the Reynolds shear stress in streamline axes, $-\overline{u'_* v'_*}$ (figure 13*c*) and in x–y axes, $-\overline{u'v'}$ (figure 13*e*). A further example is provided by what could be called the 'effective' or 'productive' stress $-\overline{u'v'}_{prod}$, formulated in terms of the mean-to-turbulence energy transfer $\mathcal{P}_k$, which is independent of axes. Since the rate of TKE production represents the work done against the mean-rate-of-strain field by the turbulent stresses, we define $-\overline{u'v'}_{prod}$ as the characteristic turbulent-shear-stress field given by the scalar ratio $\mathcal{P}_k/\sqrt{2\mathcal{S}_{ij}\mathcal{S}_{ij}}$ (which in a parallel flow, with $\overline{u} = \overline{u}(y)$, reduces to $-\overline{u'v'}$). Figure 13(*e*,*f*) implies that $-\overline{u'v'}$ and $-\overline{u'v'}_{prod}$ are very different, to the point that their outer-layer maxima are on the opposite sides of the bubble. (The $-\overline{u'v'}_{prod}$ and $-\overline{u'_* v'_*}$ fields are qualitatively similar, although not identical, especially downstream of reattachment; figure 13*f*,*c*.) Moreover, the streamline slope does not have to be extreme for the differences to be meaningful. This can be seen when examining the so-called Reynolds-stress structure parameter, $a_1 = -\overline{u'v'}/k$ (Bradshaw, Ferris & Atwell 1967). This stress/TKE ratio can be interpreted as a measure of the 'efficiency' with which the turbulence alters (transfers) the mean momentum (and energy) in a parallel flow. Figure 13(*g*) reveals the frequently observed reduction of a_1 in the APG region (Spalart & Watmuff 1993), which is typically assumed to imply a reduction in the efficiency of the turbulence/mean transfer process (e.g. Coleman *et al.* 2003). (The stress/energy ratio based on the Reynolds stress in streamline coordinates, $a_1^* = -\overline{u'_* v'_*}/k$, also reveals a downstream reduction, albeit one slower than for a_1.) In fact, the productive stress/energy ratio $a_{1,prod} = -\overline{u'v'}_{prod}/k$ (figure 13*h*) demonstrates the opposite, that the effect of the APG is an increase of relative mean-to-turbulence energy transfer – and that this increase is observed in regions where the streamline slope is quite small. Also noteworthy is the 'quiet zone of inefficiency' above the bubble, where $a_{1,prod} \approx 0.2$.

3.5. *Pressure-gradient dependence of near-wall length scales*

We now turn attention to the behaviour of various length scales associated with near-wall turbulence, and in particular how they are affected by pressure gradient. This exercise extends our work on turbulent Couette–Poiseuille (C–P) flow DNS, for which one side is effectively an APG layer, the other effectively an FPG (Johnstone, Coleman & Spalart 2010; Coleman, Garbaruk & Spalart 2015). There we found the length scale defined by the logarithmic law tends to be less sensitive to wall-normal shear-stress gradients than other alternatives. This line of thinking was initiated by

Galbraith & Head (1975) and Galbraith *et al.* (1977). The question before us now is the extent to which this parallel-flow observation also holds for the spatially developing case. The implications for turbulence modelling and theory are significant.

For context, recall that one finds in the literature at least three conjectured relationships between the wall-normal derivative of the mean velocity $\mathrm{d}U/\mathrm{d}y$ and the primary shear stress $-\overline{u'v'}$, the two quantities at the core of turbulence modelling in unidirectional flows. Based on the assumption of a constant-stress ('pure Couette') region, and presented in terms of length scales, to allow direct comparisons, these relationships include the one leading to the logarithmic law of the wall for the velocity, namely

$$\ell_U = \frac{u_\tau}{\mathrm{d}U/\mathrm{d}y} = \kappa y, \tag{3.5}$$

where κ is again the von Kármán constant and $u_\tau = \sqrt{\tau_w/\rho}$ the wall friction velocity. In terms of eddy viscosity $\nu_t \equiv -\overline{u'v'}/(\mathrm{d}U/\mathrm{d}y)$, we also have

$$\ell_{\nu_t} = \frac{\nu_t}{u_\tau} = \frac{-\overline{u'v'}/u_\tau}{\mathrm{d}U/\mathrm{d}y} = \kappa y, \tag{3.6}$$

while consideration of the mixing length $\ell_t \equiv (\nu_t/(\mathrm{d}U/\mathrm{d}y))^{1/2}$ gives

$$\ell_t = \frac{\sqrt{-\overline{u'v'}}}{\mathrm{d}U/\mathrm{d}y} = \kappa y. \tag{3.7}$$

Yet another scale can be based on the rate of TKE production (Coleman *et al.* 2015),

$$\ell_{\mathcal{P}} = \frac{u_\tau^3}{-\overline{u'v'}\mathrm{d}U/\mathrm{d}y} = \kappa y. \tag{3.8}$$

The four formulae differ by various powers of the ratio $-\overline{u'v'}/u_\tau^2$. Since $-\overline{u'v'} = u_\tau^2$ in a constant-stress layer outside the viscous region, all four expressions are equivalent under pure Couette conditions (see figure 4 in Johnstone *et al.* 2010). None of the four has a systematic derivation. (See Skote & Wallin (2016) for a review of current wall-damping functions, and an attempt to generalise them into a single model applicable to decelerating and separated flows.) With pressure gradient, $-\overline{u'v'}$ deviates from u_τ^2, even outside the viscous buffer layer, and the proposals conflict, so that at best one of the four will remain effective. The four will produce a 'fan' of results in the order (3.8)–(3.5)–(3.7)–(3.6): that is, $\ell_{\mathcal{P}} < \ell_U < \ell_t < \ell_{\nu_t}$ for APG, and $\ell_{\mathcal{P}} > \ell_U > \ell_t > \ell_{\nu_t}$ for FPG (or, in terms of ℓ_U, $(-\overline{u'v'}/u_\tau^2)^{-1}\ell_U \gtrless \ell_U \gtrless (-\overline{u'v'}/u_\tau^2)^{1/2}\ell_U \gtrless (-\overline{u'v'}/u_\tau^2)\ell_U$.) This behaviour is confirmed in figure 14, which presents (3.5)–(3.8) for Case C at representative stations (with $\mathrm{d}U/\mathrm{d}y$ replaced by local $\partial\overline{u}/\partial y$), in that ℓ_{ν_t} and $\ell_{\mathcal{P}}$ are the largest, respectively, in the APG and FPG regions. (For reference, the solid symbol in figure 14 denotes the local $0.15\widetilde{\delta}_{995}$ location, the height below which one might expect classical inertial sublayer relations to hold; cf. Marusic *et al.* 2013.) As required, the ordering is indeed tied to the magnitude of the $-\overline{u'v'}/u_\tau^2$ ratio (see shear-stress inset plots in figures 9 and 11).

Because $-\overline{u'v'}/u_\tau^2 \leqslant 1$ at the ZPG station, unlike for pure Couette flow, there is a discernible difference between the length scales here. Figure 14(*a*) reveals a mild form of the expected FPG ordering ($\ell_{\mathcal{P}}$ maximum, ℓ_{ν_t} minimum) for the Case C ZPG reference state. An even larger difference with respect to the parallel C–P geometry – for which, on both the APG and FPG sides, ℓ_U is least sensitive to $\mathrm{d}P/\mathrm{d}x$ and agrees

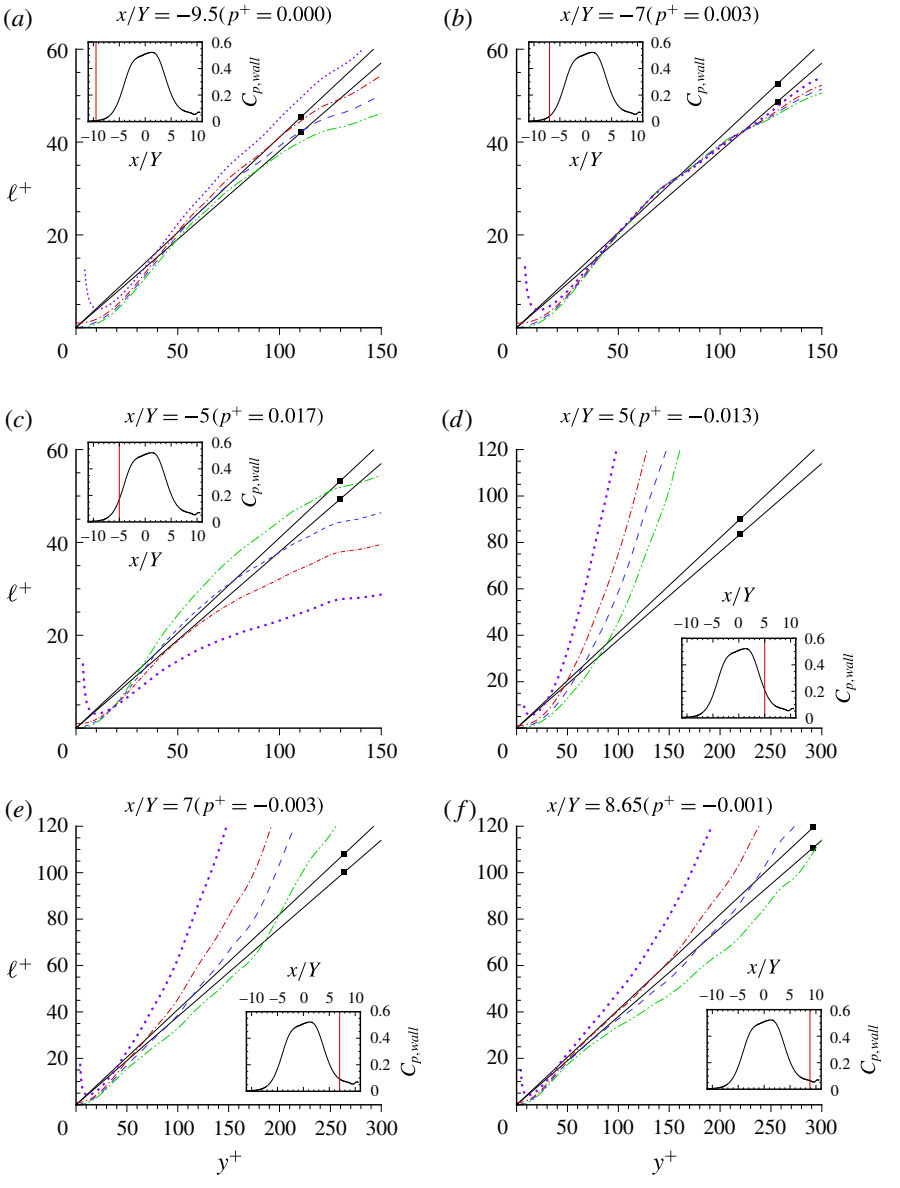

FIGURE 14. (Colour online) Length scale variation for Case C at (*a*) $x/Y = -9.5$, (*b*) $x/Y = -7$, (*c*) $x/Y = -5$, (*d*) $x/Y = 5$, (*e*) $x/Y = 7$ and (*f*) $x/Y = 8.65$: ——, κy, for $\kappa = 0.38$ and 0.41; ■, $y^+ = 0.15\, u_\tau\, \widetilde{\delta}_{995}/\nu$; — · — (red), ℓ_U; — · · — (green), ℓ_{ν_t}; - - - - (blue), ℓ_t; · · · · · · (violet), $\ell_{\mathcal{P}}$. Vertical lines in (wall-pressure) inset plots indicate streamwise station to which data in main plot correspond.

most closely with the κy idealisation (Johnstone *et al.* 2010; Coleman *et al.* 2015) – is that for the present flow the 'winner' regarding PG independence is not as clear (and is not $\ell_{\mathcal{P}}$, despite the hints found in Spalart (1988), as described in Coleman *et al.* (2015)). The prevailing uncertainty over the value of κ has essentially no impact on the comparisons. (Neither does the use of the coordinate-dependent/parallel-flow

definitions in (3.5)–(3.8): utilising the TKE-production-based quantities mentioned above instead – representing ℓ_U by $-u_\tau/\overline{\omega}_z$ or $u_\tau/(2\mathcal{S}_{ij}\mathcal{S}_{ij})^{1/2}$, ℓ_{ν_t} by $\mathcal{P}_k/(2\mathcal{S}_{ij}\mathcal{S}_{ij}u_\tau)$, ℓ_t by $\mathcal{P}_k^{1/2}/(2\mathcal{S}_{ij}\mathcal{S}_{ij})^{3/2}$ and $\ell_\mathcal{P}$ by $u_\tau^3/\mathcal{P}_k$ – has no effect on the ordering observed in figure 14, and in fact slightly amplifies the pressure-gradient dependence of all but ℓ_U.) Nevertheless, since at most of the stations the length scale fan tends to overlap most of the κy target below the $0.15\widetilde{\delta}_{995}$ limit, and since ℓ_U and ℓ_t always lie within the 'core' of the fan, a case can be made that the log-law and mixing-length scales are more resilient to pressure gradients than the other two options. We also note the importance of the (upstream) flow history in the hysteresis between the APG and FPG regions, in the tendency for the lengths to depart from κy at higher y^+ (and especially y/δ_{995}) under an adverse gradient than under a FPG of comparable (in fact slightly weaker) magnitude, measured in local wall units (compare figures 14*c* and 14*d*). At $x/Y = 5$, long after reattachment, the deviations are still strong, well below $y = 0.15\widetilde{\delta}_{995}$. At the final station, quasi-ZPG conditions are again apparent, with slightly more pronounced FPG ordering, due to the sub-ZPG levels of $-\overline{u'v'}/u_\tau^2$ mentioned in § 3.3. To appreciate the significance of these findings for RANS modelling, we note that algebraic models explicitly containing ℓ_{ν_t} or ℓ_t such as Cebeci–Smith or Baldwin–Lomax are no longer in general use, but that wall functions based on ℓ_U are in use, and also that some transport-equation models (including Spalart–Allmaras) contain terms related to ℓ_t.

4. RANS model testing

RANS solutions were computed for Case C, in an effort to explore and discern differences between RANS and DNS, as well as between RANS solutions that used different turbulence models. A similar study has been done by Raiesi *et al.* (2011), using LES at a comparable Reynolds number, but a somewhat more abrupt pressure gradient, than for Case C; their *a posteriori* RANS tests differ from those done here in that they chose to match the skin friction, rather than momentum thickness, in the upstream ZPG region. This case is also similar to the axisymmetric separated-boundary-layer experiment of Driver (1991) (coincidentally also labelled 'Case C'). The experiment and results from various RANS turbulence models can be found on the TMR website.

4.1. *RANS grid and numerical details*

Results were computed with the code CFL3D (Krist, Biedron & Rumsey 1998), developed at NASA. CFL3D is a multi-zone compressible RANS code that employs grid sequencing and multigrid to accelerate convergence to steady state. It is a finite-volume method, and uses third-order upwind-biased spatial differencing on the convective and pressure terms and second-order differencing on the viscous terms; it is globally second-order spatially accurate. The flux difference-splitting (FDS) method of Roe (1981) is employed to obtain fluxes at the cell faces. CFL3D is advanced in time via backward Euler, with an implicit three-factor approximate factorisation method. The turbulence equations are solved by default with a first-order advection scheme, although second-order is also available.

There are many RANS turbulence models available in CFL3D. For this work, we used Baldwin–Lomax (BL) (Baldwin & Lomax 1978), Spalart–Allmaras (SA) (Spalart & Allmaras 1994), Spalart–Allmaras with rotation-curvature correction (SARC) (Shur *et al.* 2000), the 'AB' k–ϵ model of Abid (k–ϵ) (Abid 1993), Menter's

shear-stress transport k–ω (SST) (Menter 1994) and the SSG/LRR-RSM-w2012 (Speziale–Sarkar–Gatski/Launder–Reece–Rodi differential Reynolds-stress model) Reynolds-stress transport (RST) (Eisfeld, Rumsey & Togiti 2016). Because of the relatively low Reynolds number of this flow, we also used modified forms of SA and SARC, termed low-*Re* SA and low-*Re* SARC, respectively. These are the same as the original models, with the exception that the coefficient C_{w2} has been increased from 0.3 to 1.0. This change yields somewhat higher skin friction for the ZPG flow leading up to separation. The original models were calibrated for higher Re, and they tend to underpredict flat-plate skin friction when Re is very low. Increasing C_{w2} in SA increases the slope of f_w with respect to $r \equiv \nu_t/(\kappa^2 y^2 \partial\overline{u}/\partial y)$ at $r = 1$ (i.e. in the log region, where $\nu_t = \kappa u_\tau y$ and $\partial\overline{u}/\partial y = u_\tau/\kappa y$), such that the SA destruction term is diminished in the outer layer, where $r < 1$ (see figure 3 of Spalart & Allmaras 1994). Consequently, the total mixing across the layer, via enhanced ν_t, increases, leading to higher skin friction.

The turbulence models are not described in detail here; the reader is referred to the original references for their equations. In terms of a general overview, BL is an algebraic model that sees very little usage today (except by the hypersonics community). It is included here because it provides an example of poor results with far too early separation (the model, however, has the opposite trend for shock-induced separation). Similarly, k–ϵ is not widely used for aerodynamic flows because of its poor characteristics, particularly for flows with APG. Here, it is included because it provides an opposite example of poor results with no separation. The other models, SA, SARC, SST and RST, are all considered state-of-the-art RANS models by today's aerodynamics community. SA and SARC are one-equation transport models, SST is a two-equation transport model, and RST is a seven-equation transport model.

The fine grid size was 721×513. Medium grid size was 361×257 (every other point of the fine grid in each coordinate direction). The grid extended from $x/Y = -12.15$ (upstream) to $x/Y = 10.65$ (downstream). The top-wall boundary was located at $y/Y = 1$. Minimum normal spacing at the bottom wall was $\Delta y/Y = 8 \times 10^{-5}$ (fine grid) and $\Delta y/Y = 16 \times 10^{-5}$ (medium grid), corresponding to an average Δy^+ over the entire plate of approximately $\Delta y^+ = 0.2$ and 0.4, respectively. Solutions computed on both grids yielded only very minor differences in results. For example, the maximum change in separation or reattachment location for any model was less than $0.2Y$, with maximum change in bubble length of approximately $0.3Y$, or less than 2 %. Therefore, medium grids were used for the solutions shown here.

The reference (ZPG free-stream) Mach number was $M = 0.1$, and Reynolds number based on the reference velocity and height Y) was $Re = 80\,000$, to agree with Case C. The top-wall condition was set by (2.2*a–c*), with $\overline{v}(x, Y) = V_{top}(x)$ and $\partial\overline{u}/\partial y|_{x,Y} = \mathrm{d}V_{top}/\mathrm{d}x|_x$, using the Case C transpiration parameters (table 1). All other mean-flow and turbulence variables had zero wall-normal gradient at $y = Y$. The streamwise location at which V_{top} changes from suction to blowing was adjusted for each model such that, at $9.5Y$ upstream of the suction/blowing-transition station (in the ZPG region), the momentum thickness agreed with that from Case C at $x = -9.5Y$ (i.e. $\widetilde{\theta}/Y = 0.022$; see figure 15*a*). For all but BL, the inflow boundary condition (BC) was set by the Case C DNS profiles of effective eddy viscosity (see below), TKE and/or Reynolds stresses at $x/Y = -12.15$. (For example, for k–ϵ, k was assigned to the DNS TKE and ϵ inferred from that k and the DNS eddy viscosity; for SA, $\widetilde{\nu}$ was computed from the $\nu_t = f_{v1}(\widetilde{\nu}/\nu)$ relation with the left-hand side set to the DNS quantity; etc.) The BL run was allowed to develop from a laminar state far upstream, such that its momentum thickness also matched the DNS at $x/Y = -9.5$.

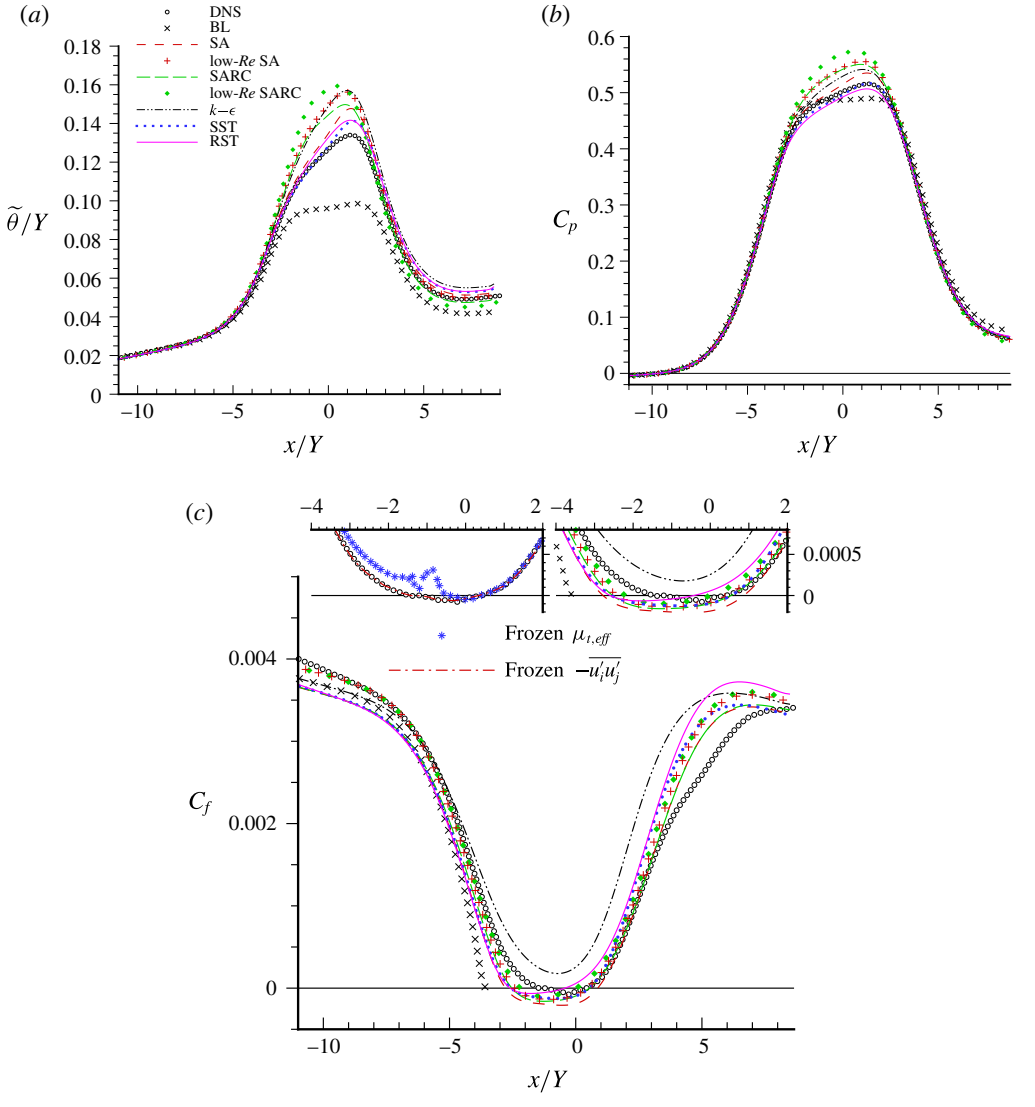

FIGURE 15. (Colour online) RANS predictions of (*a*) momentum thickness, (*b*) mean wall pressure and (*c*) skin friction for Case C. RANS models include BL (Baldwin & Lomax 1978), SA (Spalart & Allmaras 1994), low-*Re* SA (SA with $C_{w2} = 1.0$), SARC (SA with rotation/curvature correction; Shur *et al.* 2000), low-*Re* SARC (SARC with $C_{w2} = 1.0$), k–ϵ (model 'AB' of Abid 1993), SST (Menter 1994) and RST (Reynolds-stress-transport model of Eisfeld *et al.* 2016). Wall-pressure coefficient in (*b*) relative to $\overline{p}_{wall}$ at $x/Y = -9.5$. DNS results have been locally averaged in x.

Non-dimensional density was specified to be 1, and pressure was extrapolated from the interior of the domain. The outflow BC set back pressure at $p/p_{ref} = 1.00026$, and extrapolated other variables from the interior. This value of back pressure allowed the inflow Mach number to closely approximate the reference value ($M = 0.1$).

4.2. *RANS results*

RANS results for $\tilde{\theta}$, C_p, and C_f are shown in figure 15, with the eight different turbulence models compared to the DNS. By design, the RANS $\tilde{\theta}$ levels approaching separation agree well with the DNS (and thus with each other), but then the RANS results start to separate from each other near $x/Y = -3$.

The SST, RST and SA models follow the DNS data most closely, and the BL model has the largest error. For C_p, there is less visible deviation, with the two forms of SARC and the low-*Re* SA yielding the poorest agreement with DNS. Curiously, these models give among the largest θ and the most positive pressure; usually, due to displacement effects the trends are opposite, but here the models yield mean profiles with unusually small δ^* in the separation zone.

For C_f, the standard RANS model results tend to be slightly low compared to DNS in the ZPG region. This underprediction is a result of the low Reynolds number; as mentioned earlier, the RANS models are calibrated for significantly higher Reynolds numbers. The low-*Re* versions of SA and SARC were used to alleviate this deficiency in the approach flow. As shown, these two models match the DNS extremely well in this region.

Two models stand out as being particularly poor for predicting the separated flow: BL predicts separation too early, and k–ϵ predicts fully attached flow (as did another version of k–ϵ tested by Raiesi *et al.* (2011)). All other turbulence models produce fairly consistent results in terms of the separation location, near $x/Y = -2.5$. This separation location is somewhat early compared to DNS (with separation near $x/Y = -1.4$). These findings are consistent with those found from RANS tests in a parallel-flow idealisation of APG-induced separation (based on the DNS results of Coleman *et al.* (2003)), presented in Yorke & Coleman (2004) and Sciberras & Coleman (2007), in that BL separated too early, (another version of) k–ϵ not at all, and the separation predictions of SA, SST and two of three RST closures were very similar, with a tendency to be slightly too early.

The near-uniformity of RANS in prediction of separation location is somewhat surprising, considering the large differences in their eddy-viscosity fields, to be shown below, and in the structures of the various models. For the skin friction to be less sensitive than the thickness and wall pressure was also not expected.

Most models reattach between $0.5 < x/Y < 0.9$ (for a total separation bubble length near $3Y$ or more, which is too long compared to the DNS bubble length of approximately $1.85Y$). RST and low-*Re* SARC predict the shortest bubble lengths of approximately $2Y$, in better agreement with the DNS length, but the separation and reattachment locations are both too early.

The most definite deviations of C_f from the DNS are well after reattachment, near $x/Y = 5$, nearing the end of the strong FPG. For x/Y between 4 and 5, the DNS distribution has a marked reduction in slope, which all models miss before matching the DNS again around $x/Y = 8$. Again, the models cluster together even when deviating from the reference. This is a lesson in turbulence modelling: a not uncommon strategy, when concerned about the modelling errors, is to try a few models in an attempt to gauge the sensitivity of the flow. The present results show that a large number of models that can be viewed as meaningfully different from each other can err in the same manner.

Logarithmic contour plots of total, molecular μ_m plus turbulent μ_t, viscosity, in units of μ_m, are shown in figure 16, using a logarithmic scale for y, to better display near-wall behaviour. For the DNS, an 'effective' eddy viscosity is defined in terms of the

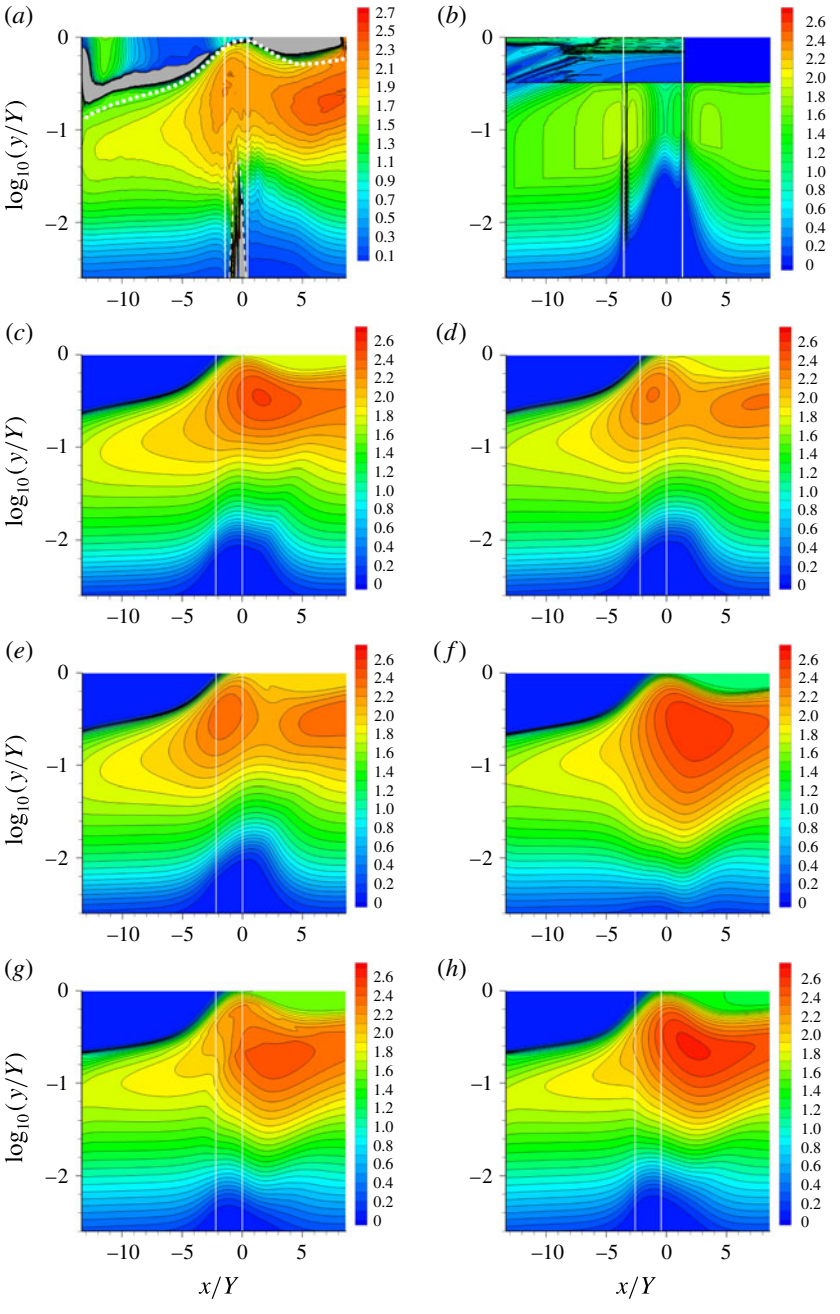

FIGURE 16. Effective and modelled eddy viscosity for Case C: (*a*) DNS; (*b*) BL (Baldwin & Lomax 1978); (*c*) SA with $C_{w2} = 1.0$; (*d*) SARC (Shur *et al.* 2000); (*e*) SARC with $C_{w2} = 1.0$; (*f*) k–ϵ (Abid 1993); (*g*) SST (Menter 1994); (*h*) RST (Eisfeld *et al.* 2016). Quantity shown is the (base-10) logarithm of $\nu_t/\nu + 1$. Note logarithmic scale of vertical axis. White solid vertical lines indicate mean separation and reattachment stations; white symbols denote 99.5 %-boundary-layer thickness $\widetilde{\delta}_{995}$. Grey/shaded regions in (*a*) correspond to $\nu_{t,eff} < 0$, and broken white curve in (*a*) is mean dividing streamline of separation bubble; DNS results have been locally averaged in x.

rates of TKE production $\mathcal{P}_k = -\overline{u_i' u_j'} \mathcal{S}_{ij}$ and mean strain $\mathcal{S}_{ij} = (1/2)(\partial \overline{u}_i/\partial x_j + \partial \overline{u}_j/\partial x_i)$ as:

$$\mu_{t,eff} = \frac{\rho \mathcal{P}_k}{2\mathcal{S}^2}, \tag{4.1}$$

where $\mathcal{S} = \sqrt{\mathcal{S}_{ij}\mathcal{S}_{ij}}$. This equation (which was also employed by Raiesi *et al.* (2011) and Abe *et al.* (2012) in their analysis of their separation-bubble simulations) follows directly from the use of the Boussinesq approximation in the definition of $\mathcal{P}_k$, for an incompressible flow. It also corresponds to a least-squares fit of the Reynolds-stress tensor by a scalar eddy viscosity. Unlike other physical quantities, such as the TKE and its rate of dissipation – which in general can be quite different from the modelling variable bearing the same name – the rate of TKE production represents the direct effect of the turbulence upon the mean flow that the model is aiming to capture. Our premise is that comparisons of eddy viscosity from each model with the $\mathcal{P}_k$-based $\mu_{t,eff}$ (4.1) from the DNS will give helpful local indications for improvement of the models.

The DNS graph indicates that a peak in non-dimensional eddy viscosity occurs above the separation bubble, with a level near 150. Then, a subsequent peak occurs well downstream, with a somewhat higher level near 250.

Above $\log_{10}(y/Y) \approx -1.5$ (i.e. $y/Y \approx 0.03$), the various RANS model eddy viscosity results vary widely. The SARC and low-*Re* SARC are closest to the DNS in this region, both in terms of levels and in the fact that a second peak occurs downstream of the bubble. This is not consistent with the thickness and pressure distributions, which were worse for the two SARC versions. The SA, SST, and RST models all produce only one peak, which is much stronger than in the DNS, and also occurs downstream of reattachment. The eddy viscosity from k–ϵ appears to be qualitatively similar to RST, which produced the highest peak value. Considering SA, SARC, SST and RST, it is at first surprising that such widely varying eddy viscosity levels all predict very similar separation locations. But looking closer to the wall (below $\log_{10}(y/Y) \approx -1.5$), we find these four models produced very similar eddy viscosities upstream of separation. (We were prompted to examine the near-wall behaviour by Professor P. Durbin.) Only two were conspicuously different: BL had higher near-wall values, and k–ϵ had the wrong slope in x. Therefore, the separation location appears to be mostly controlled by the near-wall levels of μ_t leading up to it. We also note that, near the wall for the region $[-5, 0]$, the modelled eddy viscosity develops a triangle with very weak values, apparently following streamlines in accordance with their transport equations, but the DNS eddy viscosity does not. This is observed even after correcting for the different location of flow reversal.

Three other tests were performed. First, the (smoothed-in-x) Reynolds-stress components $-\overline{u_i' u_j'}$ from the DNS were interpolated and frozen in the RANS code. In this case, when the mean flow was solved, near-perfect agreement with the DNS skin-friction coefficient was achieved, as shown in the left-hand subfigure of figure 15(c) (broken-line curve). This demonstrates the accuracy of the stress fields, the consistency of the boundary conditions used in the DNS and RANS, and the validity of the spatial resolution used for the RANS.

In a second test, the (smoothed-in-x) mean DNS velocities $\overline{u}(x, y)$ and $\overline{v}(x, y)$ were interpolated onto the RANS grid and held constant, while the various turbulence models were solved iteratively to convergence using this 'frozen' mean-flow field in the model's transport and constitutive equations (bypassing the RANS momentum equation). Resulting eddy-viscosity contours from this exercise were similar to those shown in figure 16, albeit with somewhat large magnitudes. In other words, the

RANS turbulence model fields do not change much as the result of imposition of the 'exact' DNS mean field.

Then, in a third test, the (smoothed-in-x) effective eddy viscosity field from the DNS was extrapolated to the RANS grid and frozen, and then the RANS mean flow was solved iteratively to convergence with the same boundary conditions. In this case, the predicted skin friction was poor, separating too late (with a very small bubble length) and exhibiting significant oscillations just prior to separation. This result is shown as dark star symbols in the top-left inset of figure 15(c). Oscillations can be blamed on a lack of smoothness in the DNS eddy viscosity, but its definition is in any case powerless to correct the Boussinesq approximation, so that the anisotropy of the Reynolds-stress tensor remains incorrect.

These RANS exercises unfortunately leave important questions unanswered. Apparently, the effective-eddy-viscosity field directly from DNS is not adequate for producing meaningful RANS results. At this time, we do not know if this inadequacy is due to the fact that a linear eddy viscosity is insufficient, and nonlinear terms are also required, or if the 'least-squares fit' operation to obtain an effective eddy viscosity is too crude an approximation. Future research efforts, first with nonlinear eddy-viscosity models, may try to address this issue. Another noteworthy result is that indications given by the eddy viscosity in figure 16 in the outer region are not reflected in the same direction by the wall pressure and skin friction. We do not know how to explain this behaviour, other than by reasoning that in the outer region the momentum equation is dominated by the pressure field. And finally, although the tendency for many of today's most widely used turbulence models to yield such similar results for separation appears to be mostly due to the models' similar near-wall behaviour, the effects of their very different behaviour away from the wall are not as clear. Comparison with the DNS effective eddy viscosity appears to suggest that the SARC model should be clearly better than other models, but when it comes to C_f predictions, it is not.

5. Summary and closing comments

DNS of a small family of separation bubbles were conducted, with emphasis on enlarging the domain, providing unquestionable boundary conditions and fully developed inflow states, varying the pressure gradient and raising the Reynolds number, all relative to a 1997 study. The database (available from https://turbmodels.larc.nasa.gov) is expected to allow rigorous comparisons with other DNS, LES and RANS results, and to guide turbulence theory as well as RANS modelling; concrete tests of a fair number of such models are included here. With non-trivial flow histories, it is not obvious how to isolate 'Reynolds-number effects', and a plausible approach based on extrapolating from the zero-pressure-gradient inflow region to the centre of the bubble was established. Discussions of the deviation of the flow from boundary-layer approximations are presented, and different definitions of the boundary-layer thicknesses are explored. Direction-invariant definitions of the 'structure parameter' (ratio of turbulent shear stress to turbulent kinetic energy) are proposed and found to differ noticeably from the x–y-linked definition. The manner in which the velocity profiles and other relevant length scales of the turbulence deviate from the law of the wall in favourable and relaxing pressure gradient is displayed. An unexpected finding is that the velocity profiles exactly at zero crossings of the skin friction satisfy Stratford's law based on local wall-pressure gradient and the square-root dependence, with the constants established separately in Couette–Poiseuille flow; this aspect of

turbulence theory is quite successful, and this could guide RANS-model validation. Overall, the body of knowledge derived from the DNS appears substantial and rather clear.

The findings for RANS modelling, in contrast, have puzzling aspects, and further thinking is needed. An effective eddy viscosity was extracted from the DNS fields, so as to provide a concrete and local target for the models. The exercise succeeded in the sense that the different models gave widely different eddy-viscosity distributions away from the near-wall region, with one of them coming much closer to the DNS result, presumably by capturing streamline curvature effects. It failed in the sense that with a few exceptions RANS results for wall quantities remained fairly clustered, even when they deviated appreciably from the reference. This made sense for the prediction of separation location, due to the models behaving similarly very near the wall leading up to it. But large variations in eddy viscosity further from the wall should imply much larger behavioural differences, which were not obvious. Note that the models did not all belong to a narrow class: they had one or two equations for eddy viscosity, or seven equations for the Reynolds stresses. This rules out simple explanations such as the models sharing a 'structure' in a deep way, although statements of this nature contain much opinion. It also serves as a warning against leaning too heavily upon the multiple-model-sensitivity tests often used in CFD, since a wide range of model types failed to bracket the target (in this case the point of mean separation and post-reattachment skin-friction development), and in fact converged to a common erroneous result. Curiously, although the RST model did predict a shorter separation extent than the others (in better agreement with the DNS benchmark), its overall eddy-viscosity field deviated further from the DNS than the SARC model, whose results were generally worse. A version of this latter model was adjusted in a simple-minded manner to better match the skin friction of the DNS in the region of zero pressure gradient. The reasoning was that residual low-Reynolds-number effects were not captured by any of the models. However, the result was that although this altered model matched DNS effective eddy viscosity reasonably well, it had worse results in the separation bubble, especially when combined with the curvature-corrected model. The response of the pressure distribution was the opposite of reasonable expectations. This suggests that even current computing power is not sufficient to remove low-Reynolds-number biases, but also that our understanding of even the simplest and most familiar of RANS models in even moderately complex situations is shallow.

Our short-term plans for DNS are to add a component of velocity in the z direction, with the same boundary conditions in the x–y plane, as a simple way to introduce sweep into the physics of the separation bubble. The expected failure of the 'Independence Principle', due to turbulence, will be quantified. We also speculate that swept separated flows may be somewhat easier to predict than two-dimensional separated flows for turbulence models, and a partial answer to this conjecture can be given. The intense concern of the aerodynamics community over the prediction of separation justifies sustained and coordinated DNS, experimental, theoretical and modelling efforts.

Acknowledgements

Thanks are due to Professor P. Durbin, for his advice regarding the RANS-model tests, and Dr M. Strelets, Professor I. Castro and Professor J. Weiss, who read early drafts and provided useful suggestions. This research was sponsored by the

NASA Transformational Tools and Technologies (TTT) Project of the Transformative Aeronautics Concepts Program under the Aeronautics Research Mission Directorate. Computations were performed on resources provided by the NASA Advanced Supercomputing (NAS) Division. The DNS code benefited from UK EPSRC-sponsored development work done by Dr D. Scott, of EPCC at the University of Edinburgh.

Appendix A. Fringe-zone boundary conditions

To accommodate the mean streamwise variation of a spatially developing turbulent layer in a streamwise periodic domain, the governing equations are modified by adding a velocity field $\boldsymbol{U}_2$ to the solution that is active just downstream of the entrance, and just upstream of the exit to the domain (Spalart & Watmuff 1993, SC97; § 2.1). This field acts as a mass sink that reduces the mean layer thickness; unlike in SC97, it also damps the turbulence, to prevent any large-scale structures generated by the detached shear layer above/downstream of the bubble from re-entering the domain, and corrupting the outer layer of the canonical ZPG state. The wall-normal variation of the fringe treatment has also changed from an exponential to the hyperbolic-tangent form shown below.

Letting $\boldsymbol{U}_2 = \boldsymbol{q}$, the streamwise q_1, wall-normal q_2 and spanwise q_3 components of the fringe field are written

$$q_i = \left(-V_2 \delta_{2i} \tanh\left[\left(\frac{y}{y_\alpha} \right)^2 \right] - \Upsilon \cdot (u_i - \langle u_i \rangle) \tanh\left[\left(\frac{y}{y_\beta} \right)^2 \right] \right) \cdot F(x), \tag{A 1}$$

where V_2 is the magnitude of the 'mean pulldown' velocity, δ_{ij} is the Kronecker delta, Υ is the (non-dimensional) fluctuation-damping coefficient, y_α and y_β are wall-normal length scales, u_i and $\langle u_i \rangle$ are respectively the total and spanwise mean ($k_z = 0$ mode) of $\boldsymbol{U}_1 + \boldsymbol{U}_3$; $F(x)$ is the fringe-activation function,

$$F(x) = \exp\left(-\left(\frac{x - x_{in}}{x_1} \right)^4 \right) + \exp\left(-\left(\frac{x - x_{in} - \Lambda_x}{x_1} \right)^4 \right), \tag{A 2}$$

where x_{in} is the x-coordinate of the inflow station (see table 2) and x_1 sets the streamwise extent of the fringe zone. The values used for each of these parameters (which were determined by experimentation) for Cases A–C are given in table 3.

x_1/Y	V_2/U_∞	y_α/Y	Υ	y_β/Y
1.0	1.5	0.518	2.0	0.16

TABLE 3. Fringe parameters.

Another fringe-related issue is the modification required to the top-wall transpiration profile $V_{top}(x)$, required to maintain zero net mass flux across the $y = Y$ plane. This is accomplished by injecting mass into the fringe zones to counteract the constant extraction ('bleed') velocity in (2.1), by replacing φ_{top} with $\varphi_{top} \cdot G(x)$, where

$$G(x) = 1 - \frac{\Lambda_x}{x_1 \sqrt{\pi}} \left[\exp\left(-\left(\frac{x - x_{in}}{x_1} \right)^2 \right) + \exp\left(-\left(\frac{x - x_{in} - \Lambda_x}{x_1} \right)^2 \right) \right]. \tag{A 3}$$

Appendix B. Transpiration boundary condition

This appendix, which summarises the virtual upper-wall transpiration boundary condition used in the DNS, is a simplified alternative to the fuller treatment presented in SC97. As is true of $\boldsymbol{U}_1$, the boundary-condition field $\boldsymbol{U}_3$ is both divergence-free and satisfies the no-slip condition at $y = 0$; it is also irrotational everywhere except for a layer of finite vorticity concentrated near the lower wall (required to satisfy the no-slip condition), of negligible magnitude compared to that of the computational variable, $\boldsymbol{\nabla} \times \boldsymbol{U}_1$. (The length scale y_2 (see SC97) that defines the thickness of the near-wall vorticity of $\boldsymbol{U}_3$ is $y_2/Y = 0.02$ for each of Cases A, B and C.)

We begin by recalling that the spectral DNS domain extends in the wall-normal direction from the no-slip wall at $y = 0$ into the irrotational free-stream as $y \to \infty$ (Spalart *et al.* 1991). The transpiration profile $V_{top}(x)$ is then prescribed along a virtual wall at $y = Y$ by defining the Fourier transform in x and z of $\boldsymbol{U}_3(x, y, z)$ such that, in irrotational regions, the spanwise mean (i.e. $k_z = 0$ modes) of its streamwise $\widehat{u}_3(k_x, y, k_z)$ and wall-normal $\widehat{v}_3(k_x, y, k_z)$ components are given by

$$\widehat{u}_3(k_x, y, 0) = \mathrm{i}\widehat{V}_{top}(k_x)\cosh(k_x y)/\sinh(k_x Y) \tag{B 1}$$

and

$$\widehat{v}_3(k_x, y, 0) = \widehat{V}_{top}(k_x)\sinh(k_x y)/\sinh(k_x Y), \tag{B 2}$$

where $\widehat{V}_{top}(k_x)$ is the Fourier transform of $V_{top}(x)$ and k_x is the streamwise component of the wavevector $\boldsymbol{k} = (k_x, k_z)$. (Non-zero k_z modes also contribute to $\boldsymbol{U}_3$; see SC97. The irrotational (large-y) $k_z = 0$ form shown in (B 1) and (B 2) is being considered in order to reveal the mean behaviour along $y = Y$.) Notice that (B 1) and (B 2) satisfy the divergence-free and irrotationality conditions by construction. Equation (B 2) also ensures that in regions where v_1 is inactive (as occurs at $y = Y$, when this height is well above the boundary-layer turbulence) and away from the fringe regions (such that q_2 is negligible), the desired transpiration profile is obtained, since the spanwise (and therefore the time) mean of the vertical velocity $\overline{v}$ satisfies $\overline{v}(x, Y) = V_{top}(x)$. The possibility that the vortical component $\boldsymbol{U}_1$ is non-negligible at $y = Y$, should the boundary-layer thickness become large relative to Y (as it does at some stations for the present cases) is accounted for in the general formulation in SC97. The case with $\boldsymbol{U}_1 = \boldsymbol{0}$ at $y = Y$ is examined here since it provides a straightforward illustration of the method's properties.

In addition to imposing the desired transpiration profile (2.1) at $y = Y$, $\boldsymbol{U}_3$ defines an effective irrotational/inviscid 'slip' velocity U_{slip}, by the $y = 0$ limit of (B 1), which is associated with a Gaussian-like inviscid static-pressure variation along the wall. This follows, first, from the fact that $\widehat{V}_{top} \propto \mathrm{i}\sinh(k_x Y)\,\widehat{u}_3(k_x, 0, 0)$, which implies $U_{slip} \propto \int_x V_{top}\,\mathrm{d}x$, and, second, that $V_{top}(x)$ has been defined as the derivative of a Gaussian; see figure 3(*a*,*b*).

Appendix C. Momentum integral balance

The mean integral-momentum balance for Case C is shown in figure 17(*a*), in terms of the thicknesses associated with the control volume from the surface to the transpiration plane at $y = Y$, such that integrating from the inflow station at x_{in} to an arbitrary x gives

$$\theta_1(x) + \theta_2(x) + \theta_3(x) + \theta_4(x) + \theta_5(x) = \int_{x_{in}}^{x} \frac{1}{2} C_f(\acute{x})\,\mathrm{d}\acute{x}, \tag{C 1}$$

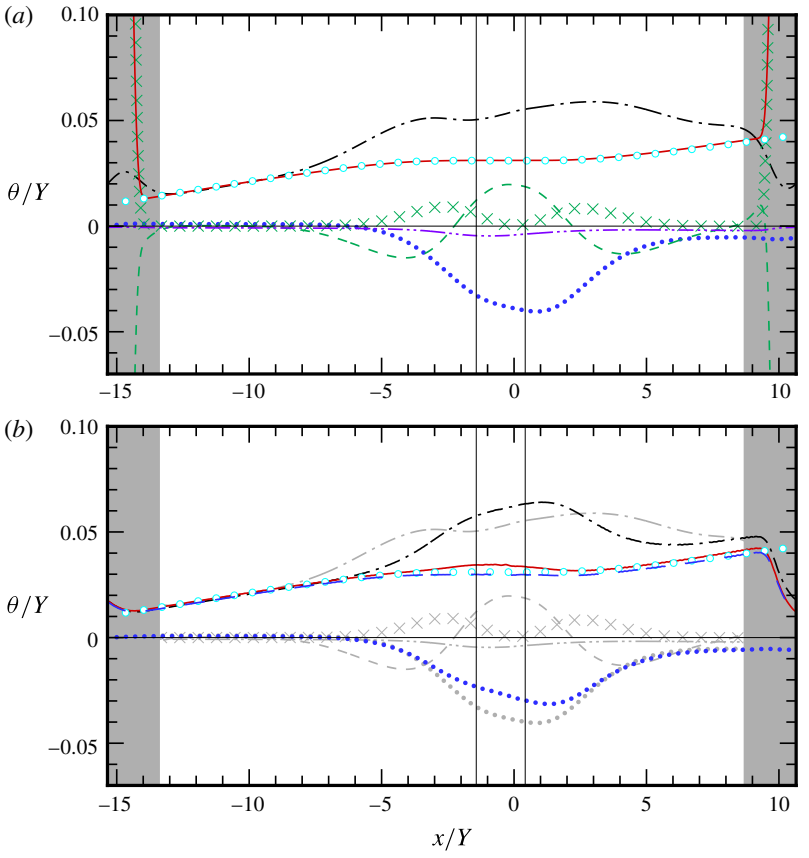

FIGURE 17. (Colour online) Integrated momentum balance for Case C. (*a*) Full balance, $y \in [0,\ Y]$ control volume: — · — (dark), θ_1; ····· (blue), θ_2; ---- (green), θ_3; × (green), θ_4; — · · — (violet), θ_5; —— (red), $\theta_1+\theta_2+\theta_3+\theta_4+\theta_5$; ○ (cyan), $\int (1/2)C_f\,\mathrm{d}x$ (shifted). (*b*) Boundary-layer approximation: — · — (dark), $(1-C_{p,wall})\,\widetilde{\theta}$; ····· (blue), $-\int (1/2)\widetilde{\delta}^*\,\mathrm{d}C_{p,wall}$; —— (red), $(1-C_{p,wall})\,\widetilde{\theta}-\int (1/2)\widetilde{\delta}^*\,\mathrm{d}C_{p,wall}$; ---- (blue), $(1-C_{p,wall})\,\widetilde{\theta}-\int (1/2)\widetilde{\delta}^*\,\mathrm{d}C_{p,wall}+\theta_5$; ○ (cyan), $\int (1/2)C_f\,\mathrm{d}x$ (shifted). Shaded/grey curves and symbols repeat results from (*a*). Vertical lines in (*a*,*b*) denote separation and reattachment locations. Grey/shaded regions indicate fringe zones. Term involving momentum thickness $\widetilde{\theta}$ in (*b*) was locally averaged in x.

where

$$\theta_1(x) \equiv \theta_U(x)\left(\frac{U_{top}(x)}{U_\infty}\right)^2 \quad \text{with } \theta_U(x) \equiv \int_0^Y \left(\frac{\overline{u}(x,y)}{U_{top}(x)}\right)\left(1-\frac{\overline{u}(x,y)}{U_{top}(x)}\right)\mathrm{d}y, \tag{C 2}$$

and

$$\theta_2(x) \equiv \int_{U_{top}(x_{in})}^{U_{top}(x)} \frac{1}{2}\delta_U^*\left(\frac{\mathrm{d}\acute{U}_{top}^2}{U_\infty^2}\right) \quad \text{with } \delta_U^*(x) \equiv \int_0^Y \left(1-\frac{\overline{u}(x,y)}{U_{top}(x)}\right)\mathrm{d}y. \tag{C 3}$$

The third term measures the deviation of the mean pressure from the top-wall value at each x,

$$\theta_3(x) \equiv \int_0^Y [(P_{top}(x) - \overline{p}(x, y))/\rho U_\infty^2] \, \mathrm{d}y, \tag{C 4}$$

while the fourth assesses the combination of (i) the stagnation-pressure loss along the top wall relative to the reference state and (ii) the deviation from one of the boundary-layer approximations, namely $V_{top}^2 \ll U_{top}^2$:

$$\theta_4(x) \equiv [P_0|_\infty - P_0|_{top}(x) + (1/2)\rho V_{top}^2(x)]Y/\rho U_\infty^2, \tag{C 5}$$

where $P_0|_\infty = P_\infty + (1/2)\rho U_\infty^2$, P_∞ is the reference static pressure (at the U_∞ location), $P_0|_{top} = P_{top} + (1/2)\rho U_{top}^2 + (1/2)\rho V_{top}^2$ and $P_{top}(x) = \overline{p}(x, Y)$. (Note that under isentropic/constant-P_0 conditions, $\theta_4 = (1/2)V_{top}^2 Y/U_\infty^2$.) The explicit effect of the turbulence is quantified by the streamwise Reynolds-stress term

$$\theta_5(x) \equiv -\int_0^Y (\overline{u'u'}(x, y)/U_\infty^2) \, \mathrm{d}y. \tag{C 6}$$

The rationale for these definitions is as follows, and aimed at generalising the von Kármán momentum equation as written within boundary-layer theory: θ_1 is the momentum deficit, and θ_2 the pressure-gradient term, containing the displacement thickness; θ_3 and θ_4 are zero and θ_5 neglected when the boundary-layer assumptions are satisfied, but non-negligible here due to the flow turning and developing non-zero $\partial\overline{u}/\partial y$ in the irrotational region (since the control volume extends to $y = Y$).

The good agreement at each x (away from the fringe zones, where the momentum sink is active) between the sum of the left-hand-side terms and the right-hand side of (C 1) displayed in figure 17(*a*) reflects well on the quality of the Case C statistics. The balance is as good or better for the other two cases.

The end of the ZPG/beginning of the APG region at $x/Y \approx -9$ is characterised by the divergence of θ_1 from the accumulated skin friction, as the pressure-deviation term θ_3 begins to have an influence. Further downstream, near $x/Y = -6$, the displacement θ_2 and stagnation-pressure θ_4 contributions become active, near the location at which the streamwise Reynolds stress begins to make a small but not insignificant contribution. (The insignificance of the stagnation-pressure loss along $y = Y$ is reflected in the near-equivalence of $(1/2)V_{top}^2 Y/U_\infty^2$ with θ_4; compare figure 3*a* and cross symbols in figure 17*a*.) The size of θ_3, the pressure-deviation integral thickness, suggests rather large wall-normal mean pressure gradients, presumably related to mean streamline divergence and/or curvature – which raises the prospect of the breakdown of the boundary-layer approximations surprisingly early in the APG layer's development.

Under the boundary-layer assumptions, θ_1 is replaced by $(1 - C_{p,wall})\,\theta$ and θ_2 by $-\int (1/2)\delta^* \, \mathrm{d}C_{p,wall}$, with $\theta_3 = \theta_4 = \theta_5 = 0$. This form is shown in figure 17(*b*), using the vorticity-based displacement and momentum thicknesses (3.3) and (3.4); the balance is better than the size of the non-ZPG terms in figure 17(*a*) might suggest. In fact, the agreement between the sum of the two boundary-layer-approximation terms and the integrated skin friction is quite reasonable, especially when the Reynolds-stress contribution θ_5 is included (dashed curve). The implication – in addition to the need to account for the streamwise Reynolds stresses to fully close the budget – is that the large $\partial\overline{p}/\partial y$ implied by the behaviour of θ_3 in figure 17(*a*) is associated with the

irrotational flow above the boundary-layer turbulence. (Recall that the displacement and momentum thicknesses used in the boundary-layer-approximation balance in figure 17*b* are defined solely by the mean spanwise vorticity within the layer.) This is underlined by the tendency for $(1 - C_{p,wall})\widetilde{\theta}$ to remain significantly smaller than θ_1 well into the APG, and that in this region θ_1 and θ_3 tend to offset each other. To conclude, it appears necessary to distinguish as many as five components in the 'extended' momentum thickness, as we did in (C 1), to account for the non-boundary-layer effects; however, the momentum balance of the DNS is then very accurate.

REFERENCES

ABE, H. 2017 Reynolds-number dependence of wall-pressure fluctuations in a pressure-induced turbulent separation bubble. *J. Fluid Mech.* **833**, 563–598.

ABE, H., MIZOBUCHI, Y., MATSUO, Y. & SPALART, P. R. 2012 DNS and modeling of a turbulent boundary layer with separation and reattachment over a range of Reynolds numbers. In *CTR Annual Research Briefs*, pp. 311–322. Stanford University, Center for Turbulence Research.

ABID, R. 1993 Evaluation of two-equation turbulence models for predicting transitional flows. *Intl J. Engng Sci.* **31** (6), 831–840.

ALAM, M. & SANDHAM, N. D. 2000 Direct numerical simulation of 'short' laminar separation bubbles with turbulent reattachment. *J. Fluid Mech.* **410**, 1–28.

ALFREDSSON, P. H., SEGALINI, A. & ÖRLÜ, R. 2011 A new scaling for the streamwise turbulence intensity in wall-bounded turbulent flows and what it tells us about the 'outer' peak. *Phys. Fluids* **23**, 041702.

BACHALO, W. D. & JOHNSON, D. A. 1986 Transonic, turbulent boundary-layer separation generated on an axisymmetric flow model. *AIAA J.* **24** (3), 437–443.

BALDWIN, B. S. & LOMAX, H. 1978 Thin-layer approximation and algebraic model for separated turbulent flows. *AIAA Paper* 78-257.

BENTALEB, Y., LARDEAU, S. & LESCHZINER, M. A. 2012 Large-eddy simulation of turbulent boundary layer separation from a rounded step. *J. Turbul.* **13** (4), 1–28.

BRADSHAW, P. 1988 Effects of extra rates of strain: review. In *Zoran Zaric Mem. Seminar, Dubrovnik.* Hemisphere.

BRADSHAW, P., FERRIS, D. H. & ATWELL, N. P. 1967 Calculation of boundary-layer development using the turbulent energy equation. *J. Fluid Mech.* **28** (3), 593–616.

CASTRO, I. P. 2015 Turbulence intensity in wall-bounded and wall-free flows. *J. Fluid Mech.* **770**, 289–304.

CASTRO, I. P. & EPIK, E. 1998 Boundary layer development after a separated region. *J. Fluid Mech.* **374**, 91–116.

CASTRO, I. P. & HAQUE, A. 1987 The structure of a turbulent shear layer bounding a separation. *J. Fluid Mech.* **179**, 439–468.

CASTRO, I. P. & ROBINS, A. G. 1977 The flow around a surface-mounted cube in uniform and turbulent streams. *J. Fluid Mech.* **79** (2), 307–335.

CEBECI, T. & BRADSHAW, P. 1977 *Momentum Transfer in Boundary Layers*, p. 197. McGraw-Hill.

CHENG, W., PULLIN, D. I. & SAMTANEY, R. 2015 Large-eddy simulation of separation and reattachment of a flat plate turbulent boundary layer. *J. Fluid Mech.* **785**, 78–108.

COLEMAN, G. N., GARBARUK, A. & SPALART, P. R. 2015 Direct numerical simulation, theories and modelling of wall turbulence with a range of pressure gradients. *Flow Turbul. Combust.* **95**, 261–276.

COLEMAN, G. N., KIM, J. & SPALART, P. R. 2003 Direct numerical simulation of a decelerated wall-bounded turbulent shear flow. *J. Fluid Mech.* **495**, 1–18.

COLEMAN, G. N., PIROZZOLI, S., QUADRIO, M. & SPALART, P. R. 2017 Direct numerical simulation and theory of a wall-bounded flow with zero skin friction. *Flow Turbul. Combust.* **99**, 553–564.

COLES, D. E. 1956 The law of the wake in the turbulent boundary layer. *J. Fluid Mech.* **1** (2), 191–226.

COLES, D. E. 1962 The turbulent boundary layer in a compressible fluid. *Rand Rep.* R403-PR, ARC 24473: Appendix A: a manual of experimental practice for low-speed flow.

DIANAT, M. & CASTRO, I. P. 1989 Measurements in separating boundary layers. *AIAA J.* **27** (6), 719–724.

DIANAT, M. & CASTRO, I. P. 1991 Turbulence in a separated boundary layer. *J. Fluid Mech.* **226**, 91–123.

DRIVER, D. M. 1991 Reynolds shear stress measurements in a separated boundary layer flow. *AIAA Paper* 91-1787.

DRIVER, D. M. & JOHNSTON, J. P. 1990 Experimental study of a three-dimensional shear-driven boundary layer with streamwise adverse pressure gradient. *NASA TM*-102211. Available from NASA Technical Reports Server (https://ntrs.nasa.gov).

DRIVER, D. M. & SEEGMILLER, H. L. 1985 Features of reattaching turbulent shear layer in divergent channel flow. *AIAA J.* **23** (2), 163–171.

DRÓZDZ, A., ELSNER, W. & DROBNIAK, S. 2015 Scaling of streamwise Reynolds stress for turbulent boundary layers with pressure gradient. *Eur. J. Mech. (*B*/Fluids)* **49**, 137–145.

EISFELD, B., RUMSEY, C. & TOGITI, V. 2016 Verification and validation of a second-moment-closure model. *AIAA J.* **54** (5), 1524–1541; Erratum: *AIAA J.* **54** (9), 2926.

GALBRAITH, R. A. MCD. & HEAD, M. R. 1975 Eddy viscosity and mixing length from measured boundary layer developments. *Aeronaut. Q.* **26**, 133–154.

GALBRAITH, R. A. MCD., SJOLANDER, S. & HEAD, M. R. 1977 Mixing length in the wall region of turbulent boundary layers. *Aeronaut. Q.* **27**, 229–242.

HUNT, J. C. R., WRAY, A. & MOIN, P. 1988 Eddies, stream, and convergence zones in turbulent flows. In *Studying Turbulence Using Numerical Simulation Databases, I: Proceedings of the 1988 Summer Program*. Stanford University, Center for Turbulence Research.

JOHNSTONE, R., COLEMAN, G. N. & SPALART, P. R. 2010 The resilience of the logarithmic law to pressure gradients: evidence from direct numerical simulation. *J. Fluid Mech.* **643**, 163–175.

KLINE, S. J., BARDINA, J. G. & STRAWN, R. C. 1983 Correlations of the detachment of two-dimensional turbulent boundary layers. *AIAA J.* **21** (1), 68–73.

KRIST, S. L., BIEDRON, R. T. & RUMSEY, C. L. 1998 CFL3D User's Manual (Version 5.0), *NASA TM*-1998-208444. Available from NASA Technical Reports Server (https://ntrs.nasa.gov).

LE, H., MOIN, P. & KIM, J. 1997 Direct numerical simulation of turbulent flow over a backward-facing step. *J. Fluid Mech.* **330**, 349–374.

LIGHTHILL, M. J. 1963 Introduction: Boundary layer theory. In *Laminar Boundary Layers* (ed. L. Rosenhead), chap. II, p. 687. Oxford University Press.

MARUSIC, I., MONTY, J. P., HULTMARK, M. & SMITS, A. J. 2013 On the logarithmic region in wall turbulence. *J. Fluid Mech.* **716**, R3.

MENTER, F. R. 1994 Two-equation eddy-viscosity turbulence models for engineering applications. *AIAA J.* **32** (8), 1598–1605.

MOHAMMED-TAIFOUR, A. 2017 Instationnarités dans une bulle de décollement turbulente: étude expérimental. PhD thesis, École de Technologie Supérieure, University of Quebec, Canada.

MOIN, P. & MAHESH, K. 1998 Direct numerical simulation: a tool in turbulence research. *Annu. Rev. Fluid Mech.* **30**, 539–578.

NA, Y. & MOIN, P. 1998 Direct numerical simulation of a separated turbulent boundary layer. *J. Fluid Mech.* **374**, 379–405.

NAUGHTON, J. W., VIKEN, S. A. & GREENBLATT, D. 2006 Skin-friction measurements on the NASA hump model. *AIAA J.* **44** (6), 1255–1265.

RAIESI, H., PIOMELLI, U. & POLLARD, A. 2011 Evaluation of turbulence models using direct numerical and large-eddy simulation data. *Trans. ASME J. Fluids Engng* **133**, 021203.

RODRIGUEZ, I., LEHMKUHL, O., CHIVA, J., BORRELL, R. & OLIVA, A. 2014 On the wake transition in the flow past a circular cylinder at critical Reynolds numbers. In *Proceedings of 11th World Congress on Computational Mechanics (WCCM XI); 5th European Conference on*

Computational Mechanics (ECCM V); 6th European Conference on Computational Fluid Dynamics (ECFD VI) (ed. E. Oñate, J. Oliver & A. Huerta).

ROE, P. L. 1981 Approximate Riemann solvers, parameter vectors, and difference schemes. *J. Comput. Phys.* **43**, 357–372.

SANDBORN, V. A. & KLINE, S. J. 1961 Flow models in boundary-layer stall inception. *Trans. ASME J. Basic Engng* **83** (3), 317–327.

SANDHAM, N. D. 2002 Introduction to direct numerical simulation. In *Closure Strategies for Turbulent and Transitional Flows* (ed. B. E. Launder & N. D. Sandham), chap. 7, p. 854. Cambridge University Press.

SCHLATTER, P. & ÖRLÜ, R. 2010 Assessment of direct numerical simulation data of turbulent boundary layers. *J. Fluid Mech.* **659**, 116–126.

SCIBERRAS, M. A. & COLEMAN, G. N. 2007 Testing of Reynolds-stress-transport closures by comparison with DNS of an idealized adverse-pressure-gradient boundary layer. *Eur. J. Mech. (B/Fluids)* **26**, 551–582.

SHUR, M. L., STRELETS, M. K., TRAVIN, A. K. & SPALART, P. R. 2000 Turbulence modeling in rotating and curved channels: assessing the Spalart–Shur correction. *AIAA J.* **38** (5), 784–792.

SIMPSON, R. L. 1989 Turbulent boundary-layer separation. *Annu. Rev. Fluid Mech.* **21**, 205–234.

SKOTE, M. & HENNINGSON, D. S. 2002 Direct numerical simulation of a separated turbulent boundary layer. *J. Fluid Mech.* **471**, 107–136.

SKOTE, M. & WALLIN, S. 2016 Near-wall damping in model predictions of separated flows. *Intl J. Comput. Fluid Dyn.* **30**, 218–230.

SLOTNICK, J., KHODADOUST, A., ALANSO, J., DARMOFAL, D., GROPP, W., LURIE, E. & MAVRIPLIS, D. 2014 CFD Vision 2030 Study: a path to revolutionary computational aerosciences. *NASA CR* 2014-218178. Available from NASA Technical Reports Server (https://ntrs.nasa.gov).

SPALART, P. R. 1988 Direct simulation of a turbulent boundary layer up to $R_\theta = 1410$. *J. Fluid Mech.* **187**, 61–98.

SPALART, P. R. & ALLMARAS, S. R. 1994 A one-equation turbulence model for aerodynamic flows. *Rech. Aerosp.* **1**, 5–21.

SPALART, P. R. & COLEMAN, G. N. 1997 Numerical study of a separation bubble with heat transfer. *Eur. J. Mech. (B/Fluids)* **16**, 169–189 (referred to herein as SC97).

SPALART, P. R., COLEMAN, G. N. & JOHNSTONE, R. 2009 Retraction: 'Direct numerical simulation of the Ekman layer: a step in Reynolds number, and cautious support for a log law with a shifted origin'. *Phys. Fluids* **21**, 109901.

SPALART, P. R., MOSER, R. D. & ROGERS, M. M. 1991 Spectral solvers for the Navier–Stokes equations with two periodic and one infinite direction. *J. Comput. Phys.* **96**, 297–324.

SPALART, P. R. & STRELETS, M. KH. 2000 Mechanisms of transition and heat transfer in a separation bubble. *J. Fluid Mech.* **403**, 329–349.

SPALART, P. R. & WATMUFF, J. H. 1993 Experimental and numerical study of a turbulent boundary layer with pressure gradients. *J. Fluid Mech.* **249**, 337–371.

STRATFORD, B. S. 1959 The prediction of separation of the turbulent boundary layer. *J. Fluid Mech.* **5**, 1–16.

UZUN, A. & MALIK, M. R. 2017 Wall-resolved large-eddy simulation of flow separation over NASA wall-mounted hump. *AIAA Paper* 2017-0538.

VINUESA, R., BOBKE, A., ÖRLÜ, R. & SCHLATTER, P. 2016 On determining characteristic length scales in pressure-gradient boundary layers. *Phys. Fluids* **28**, 055101.

WEISS, J., MOHAMMED-TAIFOUR, A. & SCHWAAB, Q. 2015 Unsteady behavior of a pressure-induced turbulent separation bubble. *AIAA J.* **53** (9), 2634–2645.

YAKHOT, A., ANOR, T., LIU, H. & NIKITIN, N. 2006 Direct numerical simulation of turbulent flow around a wall-mounted cube: spatio-temporal evolution of large-scale vortices. *J. Fluid Mech.* **566**, 1–9.

YORKE, C. P. & COLEMAN, G. N. 2004 Assessment of common turbulence models for an idealised adverse pressure gradient flow. *Eur. J. Mech. (B/Fluids)* **23**, 319–337.